### **OPEN ACCESS**



# Elemental Abundances in And XIX from Coadded Spectra

L. R. Cullinane<sup>1,2</sup>, Karoline M. Gilbert<sup>2,3</sup>, Ivanna Escala<sup>4,5,10</sup>, J. Leigh Wojno<sup>6</sup>, Evan N. Kirby<sup>7</sup>, Kateryna A. Kvasova<sup>7</sup>, Erik Tollerud<sup>3</sup>, Michelle L. M. Collins<sup>8</sup>, and R. Michael Rich<sup>9</sup>, Leibniz-Institut für Astrophysik (AIP), An der Sternwarte 16, D-14482 Potsdam, Germany; lcullinane@aip.de

The William H. Miller III Department of Physics & Astronomy, Bloomberg Center for Physics and Astronomy, Johns Hopkins University, 3400 N. Charles Street, Baltimore, MD 21218, USA

Space Telescope Science Institute, 3700 San Martin Drive, Baltimore, MD 21218, USA
 Department of Astrophysical Sciences, Princeton University, 4 Ivy Lane, Princeton, NJ 08544, USA
 The Observatories of the Carnegie Institution for Science, 813 Santa Barbara Street, Pasadena, CA 91101, USA
 Max-Planck Institute for Astronomy, Königstuhl 17, D-69117 Heidelberg, Germany
 Department of Physics and Astronomy, University of Notre Dame, 225 Nieuwland Science Hall, Notre Dame, IN 46556, USA
 Physics Department, University of Surrey, Guildford, GU2 7XH, UK
 Department of Physics and Astronomy, UCLA, Los Angeles, CA 90095, USA
 Received 2024 May 5; revised 2024 July 1; accepted 2024 July 2; published 2024 September 2

#### Abstract

With a luminosity similar to that of Milky Way dwarf spheroidal systems like Sextans, but a spatial extent similar to that of ultra-diffuse galaxies, Andromeda (And) XIX is an unusual satellite of M31. To investigate the origin of this galaxy, we measure chemical abundances for And XIX derived from medium-resolution ( $R \sim 6000$ ) spectra from the Deep Extragalactic Imaging Multi-Object Spectrograph on the Keck II telescope. We coadd 79 red giant branch stars, grouped by photometric metallicity, in order to obtain a sufficiently high signal-to-noise ratio to measure 20 [Fe/H] and [ $\alpha$ /Fe] abundances via spectral synthesis. The latter are the first such measurements for And XIX. The mean metallicity we derive for And XIX places it  $\sim \!\! 2\sigma$  higher than the present-day stellar massmetallicity relation for Local Group dwarf galaxies, potentially indicating it has experienced tidal stripping. A loss of gas and associated quenching during such a process, which prevents the extended star formation necessary to produce shallow [ $\alpha$ /Fe]–[Fe/H] gradients in massive systems, is also consistent with the steeply decreasing [ $\alpha$ /Fe]–[Fe/H] trend we observe. In combination with the diffuse structure and disturbed kinematic properties of And XIX, this suggests tidal interactions, rather than galaxy mergers, are strong contenders for its formation.

*Unified Astronomy Thesaurus concepts:* Dwarf galaxies (416); Andromeda galaxy (39); Stellar abundances (1577); Local Group (929)

Materials only available in the online version of record: machine-readable table

### 1. Introduction

First discovered in the Pan-Andromeda Archaeological Survey (PAndAS: McConnachie et al. 2008), Andromeda (And) XIX is an unusually diffuse dwarf spheriodal (dSph) satellite located 115 kpc from M31 (Conn et al. 2012). With a total luminosity of  $7.9 \times 10^5~L_{\odot}$  and a half-light radius of  $r_{\rm half} = 3065^{+935}_{-1065}$  pc (Martin et al. 2016) it is a factor of 10 more extended than similarly luminous Local Group dwarfs such as Sextans (Sex) and Carina (Car; McConnachie 2012). Its size is more comparable to ultra-diffuse galaxies (UDGs; Van Dokkum et al. 2015) in more distant galaxy clusters, but with a central surface brightness of  $\mu_{V,0} = 29.3 \pm 0.4$  mag arcsec (Martin et al. 2016) it is orders of magnitude fainter than these systems. The extended Milky Way (MW) satellite Antlia II (Ant II; Torrealba et al. 2019) is one of the only known comparably diffuse systems.

A number of different formation scenarios have been put forward to explain the observed properties of And XIX. Tidal interactions are a possibility. Both tidal shocking, where a system is impulsively heated and subsequently expands during

Original content from this work may be used under the terms of the Creative Commons Attribution 4.0 licence. Any further distribution of this work must maintain attribution to the author(s) and the title of the work, journal citation and DOI.

revirialisation (Amorisco 2019; Ogiya et al. 2022), and tidal stripping, where a loss of mass also results in revirialisation and subsequent expansion (e.g., Bennet et al. 2018; Jackson et al. 2021; Ogiya et al. 2022), are capable of significantly increasing the effective radius of satellites during pericentric passages around a massive host, particularly in galaxy clusters (Carleton et al. 2019). Indeed, the similarly diffuse Ant II is thought to have been strongly impacted by tides during a recent close pericentric passage around the MW (Ji et al. 2021).

Another proposed scenario is that strong feedback from bursty star formation dynamically heats the dark (and subsequently baryonic) matter distribution of the galaxy (e.g., Di Cintio et al. 2017; Read et al. 2019), producing a diffuse, low-density system. However, And XIX lacks the extended star formation necessary for this effect; it formed  $\sim 50\%$  of its stars 13.5 Gyr ago and 90% of its stars  $\gtrsim 10$  Gyr ago, with no indication of any star formation in the last 8 Gyr (Collins et al. 2022, henceforth C22).

A third possibility is that And XIX has been produced via galaxy mergers, with several different merger types as possible explanations. Simulations suggest that relatively high-velocity collisions between gas-rich dwarfs can produce diffuse UDG-like galaxies (Silk 2019; Shin et al. 2020; Lee et al. 2021; Otaki & Mori 2023). During these collisions, separation is induced between dark and baryonic matter, the latter of which then experiences shock compression to subsequently form stars. A strong burst of star formation in And XIX ~10 Gyr ago, during

<sup>&</sup>lt;sup>10</sup> Carnegie-Princeton Fellow.

Table 1
Observations of And XIX Used in Our Analysis, from C20

Mask Name	R.A. (h:m:s)	Decl. (d:m:s)	Position Angle (deg)	Exposure Time (s)	No. Targets Extracted	No. Targets with Usable Velocities	No. And XIX members
a19m90 <sup>a</sup>	00:19:44.69	+35:05:34.6	-90	3600	100	48	12
a19p0 <sup>b</sup>	00:19:31.02	+35:07:41.4	0	3600	103	46	5
A19S37 <sup>c</sup>	00:19:15.80	+34:56:28.3	37	3600	82	37	5
A19m1	00:19:51.00	+35:07:00.7	40	7200	102	64	17
A19m2	00:19:10.83	+34:57:23.7	40	7200	91	56	10
A1911	00:20:17.53	+35:02:58.1	40	7200	96	66	9
A1912	00:18:51.25	+35:00:15.4	40	7200	85	55	3
A19r1	00:19:39.58	+35:11:19.2	40	7200	97	52	2
A19r2	00:19:30.63	+34:58:02.8	40	7200	90	63	17
d19_1 <sup>d</sup>	00:19:30.84	+34:59:11.3	4	900	79	29	7

Notes. A total of 86 targets are considered likely And XIX members, comprising 65 unique stars, for which 18 have at least two measurements on separate masks.

which And XIX formed  $\sim$ 40% of its stars (C22), is consistent with the expected post-collision starburst in this scenario.

In alternative merger-related scenarios, simulations show that several "dry" (i.e., gas-poor) mergers between smaller satellites, each quenched by reionization, can build diffuse galaxies by depositing stars in the outskirts of the primary galaxy (Rey et al. 2019). So-called tidal dwarf galaxies (TDGs), formed from overdensities in the debris of gas-rich galaxy mergers which become self-gravitating (e.g., Duc et al. 2014; Bennet et al. 2018; Ploeckinger et al. 2018), can also be diffuse and UDG-like.

Abundance measurements—and in particular the abundances of  $\alpha$  elements (e.g., Mg, Ca, Si, Ti) relative to iron—can help distinguish between these scenarios. Type II (core-collapse) supernovae (SNe) are a significant source of  $\alpha$ -element production, while the ejecta of Type Ia SNe (SNIa) are comparatively much richer in iron. As these two processes have differing timescales, the relative abundances of  $[\alpha/Fe]$  versus [Fe/H] allow us to trace the enrichment history and star formation timescales within a galaxy (e.g., Tinsley 1979; Gilmore & Wyse 1991), and identify the remnants of accreted systems (e.g., Font et al. 2011; Naidu et al. 2020).

For example, if And XIX is produced via high-velocity galaxy collisions, it should be relatively rich in  $\alpha$  elements due to vigorous star formation immediately following the collision, during which Type II SNe dominate (Silk 2019). In contrast, if a significant fraction of And XIX's mass has been tidally stripped, it is expected to be more metal-rich than predicted by the present-day stellar mass—metallicity relation for Local Group dwarf galaxies (Kirby et al. 2013, 2020), but should have a comparable  $\alpha$ -element distribution to other dSph systems of similar original luminosity.

However, And XIX's significant distance  $(821^{+32}_{-108} \text{ kpc};$  Conn et al. 2012) makes detailed abundance measurements difficult; the only [Fe/H] abundances determined to date are presented in Collins et al. (2020, henceforth C20). They derive a mean [Fe/H] of  $-2.07 \pm 0.02$  for the galaxy by measuring the strength of the infrared Ca II triplet (which is empirically correlated with [Fe/H] for red giant branch, RGB, stars; e.g., Armandroff & Da Costa 1991) for a coadded spectrum of 81 member stars. However, the low signal-to-noise ratio (S/N) of

the individual stars implies a larger uncertainty than the 0.02 dex implied by their fitting procedure (C20).

In this paper, we present the first  $\alpha$ -element abundance measurements for And XIX, derived from spectral synthesis modeling of coadded medium-resolution spectra. This is a technique that has previously been successfully applied to low-S/N spectra of stars in other M31 satellites (Wojno et al. 2020). We outline the data used and our selection of And XIX member stars in Section 2. The details of the abundance measurement procedure, including coaddition of spectra, are given in Section 3. Section 4 presents our results, and we discuss their implications for And XIX's formation in Section 5. We conclude in Section 6.

# 2. Data

We utilize observations from a multiyear spectroscopic campaign targeting And XIX using the Deep Extragalactic Imaging Multi-Object Spectrograph (DEIMOS; Faber et al. 2003) on the Keck II 10 m telescope, as described in C20, with the addition of one previously unpublished pilot mask from the same campaign ("d19\_1"). All data are taken with the  $12001\,\mathrm{mm}^{-1}$  grating ( $R\sim6000$ ), with a central wavelength of 8000 Å, and the OG550 filter, which combined provides wavelength coverage from ~6000 to 9000 Å. Targets were selected from deep Subaru Suprime-Cam imaging as outlined in that paper. We rereduce the raw spectroscopic data using the SPEC2D and SPEC1D pipelines (Cooper et al. 2012; Newman et al. 2013), the process of which includes includes flatfielding, sky subtraction, extraction of 1D spectra, and measurement of the line-of-sight (LOS) velocity for each object via cross-correlation against template spectra (Simon & Geha 2007), so that the reduced data outputs are consistent with those that were used to calibrate our abundance measurement pipelines (described in Section 3). Since this reduction is different from that of C20, we utilize a somewhat different (though largely overlapping) sample of stars from that of C20; Table 1 (analogous to Table 1 of C20) presents an overview of the data used in our analysis, and Figure 1 presents the on-sky positions of the DEIMOS masks (black rectangles) used in our analysis, overlaid on a PAndAS stellar density map of And XIX (McConnachie et al. 2018). Since we are using independent data reductions, we derive our own velocity

<sup>&</sup>lt;sup>a</sup> Referred to as 7A19a in C20.

<sup>&</sup>lt;sup>b</sup> Referred to as 7A19b in C20.

<sup>&</sup>lt;sup>c</sup> Referred to as 8A19c in C20.

<sup>&</sup>lt;sup>d</sup> Not published in C20.

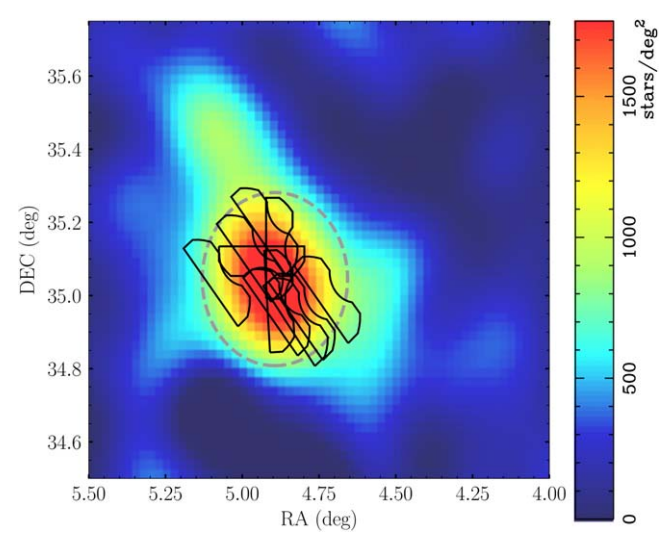


Figure 1. PAndAS density map of And XIX, taken from Figure 2 of C20. Each black outline approximates the shape of a DEIMOS slitmask used in our analysis (several of which overlap, allowing repeated observations of some stars); the dashed gray ellipse indicates And XIX's half-light radius ( $\sim$ 14'; Martin et al. 2016).

estimates (Section 2.1) and And XIX membership probabilities (Section 2.2), including removal of foreground contaminants (Section 2.3) for each star; we discuss differences between our final sample and that of C20 in Section 2.4.

#### 2.1. Velocity Measurements

We apply a number of corrections to the initial velocity measurement produced from the SPEC1D reduction in order to obtain the final velocity used in our And XIX membership model. The first of these is conversion to the heliocentric frame. Additionally, in order to account for possible miscentering of stars within each slit, which manifests as a velocity offset, we measure the systematic variation of the observed wavelength of the atmospheric A-band absorption feature (at ~7600 Å) as a function of slit position on each individual mask. We fit this "A-band correction" (Sohn et al. 2007) using a polynomial function for stars which have reliable velocity estimates on each mask, and subsequently apply it to all stars on the mask (as described by Quirk et al. 2022). In total, we obtain reliable velocity measurements for 516 targets.

Velocity uncertainties are estimated by summing in quadrature the uncertainty estimated by the velocity cross-correlation routine, and a systematic uncertainty of  $2.2\,\mathrm{km\,s^{-1}}$  (derived from data reduced using the same pipeline as we use; Simon & Geha 2007). This is slightly smaller than the systematic uncertainty floor of  $3.2\,\mathrm{km\,s^{-1}}$  derived by C20 through analysis of stars which have repeated observations across different masks. We do, however, check our velocity uncertainties are reasonable through a simpler analysis of duplicate observations within our data set; out of a total of 430 unique stars in our sample, 70 have at least two reliable velocity measurements. We calculate the LOS velocity difference between paired observations of each star with duplicate observations, scaled by the associated velocity uncertainty (i.e.,  $\frac{v_{i,1}-v_{i,2}}{\sqrt{\sigma_{v_{i,1}}^2+\sigma_{v_{i,2}}^2}}$ ). The resulting distribution has a

standard deviation of  $\sim$ 1.08, indicating our velocity uncertainties are at worst only mildly underestimated.

### 2.2. And XIX Membership Model

As we have an independent data-reduction process and velocity-determination procedure to that of C20, we independently calculate the probability of each star being associated with And XIX, largely following the procedure in Section 3.1 of C20, which we briefly outline below. Our method only differs in the thresholds used to define And XIX membership; we note where these differ below, and discuss the effects of these different selections further in Section 2.4 and the Appendix.

The total probability of a given star i being associated with And XIX,  $P_{\text{tot.}}$  is given by Equation (1):

$$P_{\text{tot},i} = P_{\text{CMD},i} \times P_{\text{vel},i} \times P_{\text{dist},i}. \tag{1}$$

Here,  $P_{\rm CMD}$  is calculated based on the star's position on the dereddened (V-i) color–magnitude diagram (CMD) relative to a PARSEC isochrone of age 12 Gyr and  $[{\rm Fe/H}] = -1.8$  (Bressan et al. 2012), shifted to a distance modulus of m-M=24.75 (Conn et al. 2012). This is the same isochrone used in C20; while C22 suggest an isochrone of 13.5 Gyr is potentially more appropriate given this corresponds to the 50% of the star formation in And XIX, the difference in position between these two isochrones is small and negligibly affects the calculated probabilities. We calculate the minimum Cartesian distance from a star to the isochrone locus,  $d_{\rm min}$ , and subsequently calculate  $P_{\rm CMD}$  using Equation (2), where  $\sigma_{\rm CMD}=0.1$  to match C20:

$$P_{\text{CMD},i} = \exp\left(\frac{-d_{\min}^2}{2\sigma_{\text{CMD}}^2}\right). \tag{2}$$

While the use of an 12 Gyr isochrone may preclude potential younger ( $\lesssim$ 6 Gyr) And XIX populations as being selected as likely member stars, given C22 find And XIX has experienced no star formation within the past  $\sim$ 8 Gyr, we consider it unlikely many, if any, genuine And XIX members are lost as a result of this selection. We do test excluding  $P_{\rm CMD}$  from the final calculation, but find the additional stars considered as potential members are located far from any RGB locus (regardless of assumed age), and therefore either clear interlopers, or at minimum outside the range for which we can determine photometric parameter estimates (a prerequisite for abundance determination in our method; see Section 3.1).

 $P_{\rm dist}$  is calculated based on the star's on-sky location, such that stars closer to the center of the dwarf are given a higher probability of being associated with it. We first calculate the distance R of each star, in arcminutes, from the center of And XIX (taken as  $0^{\rm h}19^{\rm m}34^{\rm s}5$ ,  $35^{\rm d}02^{\rm m}41^{\rm s}5$  from C20), factoring in the (nonspherical) shape of And XIX, using Equation (3) (Equation (5) of Martin et al. 2016):

$$R_{i} = \left( \left[ \frac{1}{1+\epsilon} \times (x_{i}\cos(\theta) - y_{i}\sin(\theta)) \right]^{2} + (x_{i}\sin(\theta) + y_{i}\cos(\theta))^{2} \right)^{0.5}.$$
 (3)

Here, x and y are given by Equations (4)–(5), where  $\alpha_i$ ,  $\delta_i$  are the on-sky positions of the star, and  $\alpha_0$ ,  $\delta_0$  are the on-sky

<sup>&</sup>lt;sup>11</sup> That is, for which visual inspection of the spectra suggests a reasonable velocity has been found using the cross-correlation process.

coordinates of And XIX's center:

$$x_i = -\cos(\delta_i)\sin(\alpha_i - \alpha_0), \tag{4}$$

$$y_i = \sin(\delta_i)\cos(\delta_0) - \cos(\delta_i)\sin(\delta_0)\cos(\alpha_i - \alpha_0).$$
 (5)

Here,  $\theta$  and  $\epsilon$  are structural parameters which describe And XIX's shape;  $\epsilon$  describes the ellipticity of the system and is linked to the ratio of the major (a) and minor (b) axes via  $\epsilon = 1 - b/a$ , and  $\theta$  describes the position angle of the system's major axis, measured east of north. We also adjust And XIX's half-light radius for these parameters using Equation (6). We hold these values fixed, with  $\theta = 34$  deg,  $\epsilon = 0.58$ , and  $r_{\text{half}} = 14!2$  (Martin et al. 2016):

$$r_h = r_{\text{half}} \times \frac{1 - \epsilon}{1 + \epsilon \cos(\theta)}.$$
 (6)

 $P_{
m dist}$  is subsequently calculated using Equation (7). However, we note that as the half-light radius of And XIX is relatively large compared to the on-sky area covered by a single DEIMOS spectroscopic mask (as in Figure 1),  $P_{
m dist}$  is relatively uninformative and excluding it in the final calculation does not change which stars are considered likely And XIX members:

$$P_{\text{dist},i} = \exp\left(\frac{-R_i^2}{2r_h^2}\right). \tag{7}$$

 $P_{\rm vel}$  is calculated based on the corrected LOS velocity of the stars, accounting for the underlying contamination of both MW foreground stars and the extended halo of M31. We fit the total LOS velocity distribution of our sample as the sum of three Gaussian components, per Equations (8)–(10). Here,  $\eta$  describes the fraction of stars in the sample associated with each of the three components, such that  $\eta_{\rm A19} + \eta_{\rm MW} + \eta_{\rm M31} = 1$ :

$$P_{\text{A19},i} = \frac{\eta_{\text{A19}}}{\sqrt{2\pi(\sigma_{v,i}^2 + \sigma_{0,\text{A19}}^2)}} \exp\left(\frac{-0.5(v_i - \mu_{\text{A19}})^2}{\sigma_{v,i}^2 + \sigma_{0,\text{A19}}^2}\right), \quad (8)$$

$$P_{\text{MW},i} = \frac{\eta_{\text{MW}}}{\sqrt{2\pi(\sigma_{v,i}^2 + \sigma_{0,\text{MW}}^2)}} \exp\left(\frac{-0.5(v_i - \mu_{\text{MW}})^2}{\sigma_{v,i}^2 + \sigma_{0,\text{MW}}^2}\right), (9)$$

$$P_{\text{M31},i} = \frac{\eta_{\text{M31}}}{\sqrt{2\pi(\sigma_{\nu,i}^2 + \sigma_{0,\text{M31}}^2)}} \exp\left(\frac{-0.5(\nu_i - \mu_{\text{M31}})^2}{\sigma_{\nu,i}^2 + \sigma_{0,\text{M31}}^2}\right). \tag{10}$$

While a single Gaussian is an oversimplification of the velocity distribution of MW stars, given the large distance and correspondingly relatively small on-sky area covered by And XIX, it is sufficient for our purposes of probabilistically identifying And XIX member stars. The overall likelihood function is then given by Equation (11):

$$\log(\mathcal{L}) = \sum_{i} \log (P_{A19,i} + P_{MW,i} + P_{M31,i}).$$
 (11)

We use EMCEE (Foreman-Mackey et al. 2013) to sample the posterior distribution of the model parameters and maximize the log-likelihood in Equation (11), using uniform priors (given in Table 2 of C20) for each parameter. We then normalize the probability of a star belonging to any of these three components using Equation (12) to obtain  $P_{\rm vel}$ , taking the 50th percentile of

the resulting parameter distributions in the calculation:

$$P_{\text{vel},i} = \frac{P_{\text{A19},i}}{P_{\text{A19},i} + P_{\text{MW},i} + P_{\text{M31},i}}.$$
 (12)

We choose to classify any stars which have  $P_{\text{tot}} > 0.5$  as potential members of And XIX. This is a somewhat stricter cut than C20, who use a threshold of  $P_{\text{tot}} > 0.1$  to select And XIX members; we discuss the effect of this difference in Section 2.4. There are a total of 98 targets we consider to be potential members, encompassing 76 unique stars, including 19 for which we have at least two independent measurements on different masks. We demonstrate the results of the membership selection in Figure 2 (see Figures 3 and 4 of C20). The top-right panel shows the Suprime-Cam CMD of the stars, with the thin orange line indicating the PARSEC isochrone used to derive  $P_{\rm CMD}$ . The top-left panel plots the velocity distribution for all stars as a function of their radial distance from the center of And XIX. In both panels, stars that are considered potential And XIX members are colorcoded by their membership probability  $P_{\text{tot}}$ , while nonmembers are indicated as gray dots. The bottom-left panel presents a LOS velocity histogram of all targets (gray) and those which we classify as likely members (orange); we overlay the best-fitting models of And XIX (green), M31 (purple), and the MW (blue) used to derive  $P_{\text{vel}}$ .

## 2.3. Identifying Foreground Contaminants

In addition to isolating likely And XIX member stars through the above probability-based cuts, we remove further potential MW contaminants by measuring the equivalent width (EW) of the surface-gravity-sensitive Na I doublet at 8183 and 8195 Å: Stars with strong Na I absorption are more likely to be MW foreground dwarfs compared to distant And XIX giants (e.g., Gilbert et al. 2006). We measure the EWs of the two Na I lines in windows of 8180-8190 Å and 8190-8200 Å, and sum these to obtain a total Na I EW measurement,  $\Gamma$ . We bootstrap this measurement by resampling each pixel in these two windows within its uncertainty, and measuring the associated EWs of the lines 1000 times; we take the median and standard deviation of the resulting distribution as our final  $\Gamma$  value and its uncertainty, respectively. In some cases,  $\Gamma < 0$ ; this occurs in low-S/N spectra where there are no distinct absorption lines in our measurement windows, and instead the mean flux values are above that of the nominal continuum level.

We use the "significance" of the Na I detection,  $\Gamma/\sigma_{\Gamma}$ , as an additional membership criterion. C20 apply a comparable criterion of  $\Gamma < 2$  to remove potential foreground contaminants and identify And XIX members; we discuss the effect of this different criterion further in Section 2.4. The bottom-right panel of Figure 2 shows the  $\Gamma/\sigma_{\Gamma}$  distribution for the entire sample (gray) and just those stars with  $P_{\text{tot}} > 0.5$  (orange). The majority of likely member stars have  $\Gamma/\sigma_{\Gamma} \leqslant 0.2$ , in a fairly symmetric distribution; we therefore exclude stars that do not pass this criterion from our sample of And XIX members. While a "significance" of 0.2 is relatively low to consider a detection, this is driven by the very large uncertainties on the  $\Gamma$  measurement for all stars due to their low underlying S/N; even spectra where the Na I doublet is clearly visible are sometimes only detected at a significance of 0.5 or less. Visual

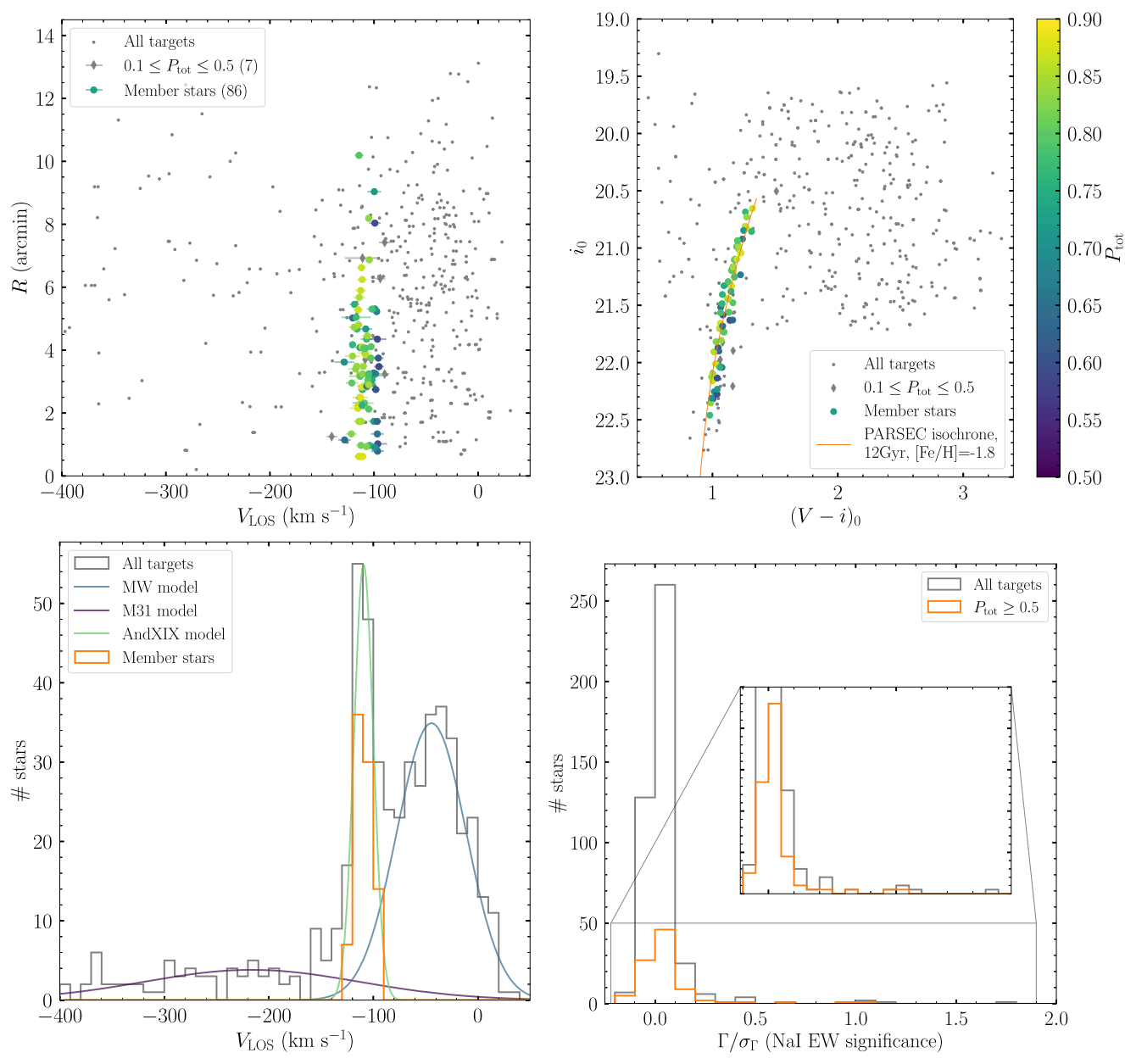


Figure 2. Top left: LOS velocity of all targets as a function of distance R, in arcminutes, from the center of And XIX. And XIX member stars have velocity uncertainties indicated with error bars. Top right: Subaru Suprime-Cam CMD of all targets. The thin orange line indicates the old, metal-poor PARSEC isochrone used to calculate  $P_{\text{CMD}}$ . In both upper panels, And XIX member stars (which pass our  $\Gamma/\sigma_{\Gamma}$  cut; see Section 2.3) are color-coded by their total membership probability, based on CMD position (Equation (2)), LOS velocity (Equation (12)), and on-sky position (Equation (7)). Stars with membership probabilities  $0.1 \le P_{\text{tot}} \le 0.5$  are indicated by diamond-shaped points. Bottom left: LOS velocity histogram for all targets (gray) and And XIX member stars (orange). Even in the full sample, a clear peak around And XIX's systemic LOS velocity ( $\sim -110 \text{ km s}^{-1}$ ) is observed. Thin colored lines indicate the fitted velocity distributions of And XIX (green), as well as potential contaminant populations from the MW (blue) and M31 (purple) used to derive  $P_{\text{vel}}$ . Bottom right: histogram of Na I doublet detection significance (i.e.,  $\Gamma/\sigma_{\Gamma}$ ) for all targets (gray) and targets with  $P_{\text{tot}} > 0.5$  (orange). We impose a cut at  $\Gamma/\sigma_{\Gamma} < 0.2$  to select likely And XIX member stars (see Section 2.3).

inspection confirms that none of the likely And XIX members which do pass the  $\Gamma/\sigma_{\Gamma}$  cut have strong Na I absorption.

In total, 86 targets pass the  $\Gamma/\sigma_{\Gamma}$  cuts and are considered as likely And XIX members; these comprise 65 unique stars, 18 of which have at least two independent measurements. When considering stars with repeated observations on different masks, in the vast majority of cases all observations are classified consistently. We find only one star for which membership disagrees between observations, due to differing velocity measurements. As both observations have low S/N, and it is not clear that either is more correct than the other, we exclude this star from further analysis as a potential member.

# 2.4. Sample Comparison to C20

Our sample of And XIX members is different to that of C20 due to several factors. In addition to a different underlying target sample, due to the differing reduction methods for the spectroscopic data, we additionally use different selection criteria to define And XIX membership. We briefly discuss the resulting differences in our samples here, with a more detailed analysis given in the Appendix.

There are seven targets which have total membership probabilities  $0.1 \leqslant P_{\rm tot} \leqslant 0.5$  and which pass our  $\Gamma/\sigma_{\Gamma}$  cut that we do not consider members, but which would be classified as members according to the  $P_{\rm tot}$  membership criteria

 Table 2

 Summary of Likely And XIX Members in This Analysis

Group	No. Targets	No. Unique Stars	No. Stars with Duplicate Observations
$P_{\text{tot}} > 0.5$	98	76	19
Likely And XIX members (i.e., $P_{\text{tot}} > 0.5 \& \Gamma/\sigma_{\Gamma} < 0.2$ )	86	65	18
Primary subsample	68	53	12
C20 $\Gamma$ difference subsample	18	12	6
Low-probability subsample	7	7	0
	In Final Coad	ds	
Primary subsample	61	49	12
C20 $\Gamma$ difference subsample	13	9	4
Low-probability subsample	5	5	0

in C20. We define these stars as a "low-probability" subsample, and coadd them separately in order to minimize any potential effects from nonmember contamination on our primary sample of likely And XIX members. There are eight targets that we classify as And XIX members but are rejected by C20 on the basis of  $P_{\rm tot} < 0.1$  due to differing velocity measurements for the stars. These spectra are relatively noisy, and it seems plausible that the different reduction pipelines simply result in different derived velocities for these targets. However, as manual inspection suggests our derived velocities are reasonable, we maintain our classification of these targets as potential And XIX members.

We additionally classify 12 targets as potential And XIX members that C20 exclude on the basis of a Na I EW measurement exceeding a  $\Gamma < 2$  cutoff, which is slightly different to the  $\Gamma/\sigma_{\Gamma} > 0.2$  we use. Six of these targets are duplicate observations, where the other observation either passes the C20  $\Gamma < 2$  cutoff, or is not successfully reduced by their pipeline. We isolate those 18 targets into a third group—our "C20  $\Gamma$  difference" sample—and, like our low-probability sample, coadd these stars separately to avoid any potential bias of results.  $^{12}$  C20 also classify an additional three targets as likely members which we do not; we exclude two targets based on  $P_{\rm tot} < 0.1$  and one based on  $\Gamma/\sigma_{\Gamma} > 0.2$ . In all cases these are relatively low-S/N spectra, which we speculate produce different results given the different reduction pipelines.

Table 2 summarizes the number of stars in each of our And XIX member subsamples, and Table 3 presents the properties of all targets for which we can measure a radial velocity, including their membership probabilities, and photometric stellar parameters ( $T_{\rm eff,phot}$ ,  $\log(g)_{\rm phot}$ , and  $[{\rm Fe/H}]_{\rm phot}$ ) for potential And XIX members in any subsample. A small number of targets do not have measured Na I EWs, where this measurement failed due to a combination of very low S/N and the presence of poorly subtracted sky lines. These targets generally lie outside the range of the isochrone grid we use to derive photometric parameter estimates (see Section 3.1), and therefore could not be used for subsequent abundance derivation even if they are potentially genuine And XIX members.

# 3. Spectroscopic Abundance Measurements

Our overall abundance determination method generally follows that in Wojno et al. (2023). We first derive photometric estimates (Section 3.1) of effective temperature ( $T_{\rm eff,phot}$ ),

surface gravity  $(\log(g)_{\text{phot}})$ , and metallicity  $([\text{Fe/H}]_{\text{phot}})$ , and use these as initial estimates in the pipeline developed by Escala et al. (2019) to obtain [Fe/H] and  $[\alpha/\text{Fe}]$  measurements for each individual stellar spectrum by comparison to a grid of synthetic spectra (Section 3.2). However, as our targets are faint, we subsequently coadd spectra as in Wojno et al. (2020, 2023) and measure average [Fe/H] and  $[\alpha/\text{Fe}]$  abundances for groups of several stars (Section 3.3). Previous work (Wojno et al. 2020) has shown these coadded measurements accurately reflect the weighted average of the underlying values of the individual contributing component stars, and that the method provides comparable abundance distributions to those derived from individual stars using both low- (Wojno et al. 2020) and high-resolution spectroscopy (Escala et al. 2019).

# 3.1. Photometric Parameter Estimates

We compare the dereddened Suprime-Cam photometry of each individual star to a grid of PARSEC isochrones (Bressan et al. 2012) in order to derive photometric stellar parameter estimates. 13 We assume an age of 13 Gyr as this is close to the 13.5 Gyr at which 50% of the star formation in And XIX is complete (C22); at ages older than 13 Gyr, a handful of stars are located beyond the low-metallicity bound of the isochrones ([M/H] = -2.2) and thus do not have reliable stellar parameter estimates. During subsequent spectral abundance measurements, the effective temperature and surface gravity for each star are held fixed at the values derived from photometry. While using a single isochrone age will impact the derived photometric parameters due to the age-metallicity degeneracy, we find varying the isochrone age between 10 and 14 Gyr has a minimal effect on our results (see Section 4.1), and, per Section 2.2, it is unlikely that there are significantly younger populations in And XIX for which the derived photometric parameters are significantly inaccurate.

We note that the PARSEC isochrones used are solar scaled (i.e., assume  $\lceil \alpha/\text{Fe} \rceil = 0$ ), which can potentially affect the derived photometric parameters and therefore the resulting spectroscopic abundances. However, Kirby et al. (2008) and Vargas et al. (2014)—both of whom use very similar methods to that of our analysis—find that photometric effective temperature and surface gravity are largely insensitive to using  $\alpha$ -enhanced isochrones up to  $\lceil \alpha/\text{Fe} \rceil = 0.3$ –0.4, and this therefore negligibly affects the derived spectroscopic abundances.

The 12 targets and the six corresponding duplicate observations.

<sup>13</sup> Version 3.6, accessed via http://stev.oapd.inaf.it/cgi-bin/cmd.

ID	R.A. (h:m:s)	Decl. (d:m:s)	Mask	V-mag	<i>i</i> -mag	$V_{\rm LOS} \ ({\rm km\ s}^{-1})$	$P_{\text{tot}}$	Γ	T <sub>eff,phot</sub> (K)	$log(g)_{phot}$ (cm s <sup>-2</sup> )	[Fe/H] <sub>phot</sub>
and19_00026	0:19:22.69	+35:02:15.3	a19m90	$22.331 \pm 0.011$	$21.166 \pm 0.006$	$-100.14 \pm 4.67$	0.73	$-2.3 \pm 28.1$	$4511 \pm 54$	$0.86 \pm 0.06$	$-1.95 \pm 0.24$
a19_00395	0:18:51.46	+35:00:37.2	A1912	$23.575 \pm 0.032$	$22.629 \pm 0.017$	$-148.20 \pm 7.52$	0.06	$7.4 \pm 6.8$			
1233	0:19:24.95	+34:58:44.1	d19_1	$22.461 \pm 0.013$	$21.497 \pm 0.007$	$-115.22 \pm 7.35$	0.30	•••	•••	•••	•••

Notes. V-mag and i-mag are extinction-corrected Vega magnitudes.  $P_{tot}$  is the combined probability of a star being associated with And XIX (see Section 2.2).  $\Gamma$  is the EW of the Na I doublet (see Section 2.3), where this is possible to measure.  $T_{eff,phot}$ ,  $log(g)_{phot}$ , and  $[Fe/H]_{phot}$  are derived from a grid of PARSEC isochrones assuming an age of 13 Gyr (see Section 3.1); these are only included for stars considered potential And XIX members.

(This table is available in its entirety in machine-readable form in the online article.)

Despite the relatively narrow CMD concentration of likely And XIX members, as seen in the upper-right panel of Figure 2, the photometric metallicities we derive for these stars show a moderate spread, spanning a range  $-2.2 \lesssim [Fe/H] \lesssim -1.4$ . This is comparable to the range of metallicities later derived using our spectroscopic pipeline (Section 4). Stars in the low-probability subsample span a comparably wide metallicity range, with 1-2 stars reaching photometric metallicities as metal-rich as  $[Fe/H] \sim -1$ . This may indicate these stars are potential interlopers from the MW or M31. However, as these values are only used as an initial estimate for our spectroscopic pipeline, which provides better constraints, we proceed with their analysis.

### 3.2. Synthetic Spectra

To obtain abundance estimates for the stars, we compare the observed 1D spectra to a grid of synthetic spectra generated by the spectral synthesis code MOOG (Sneden et al. 1997), utilizing ATLAS9 stellar atmospheric models (Kirby 2011, and references therein). The mixing length parameter for these models is  $l/H_p = 1.25$ . The associated line list draws from the Vienna Atomic Line Database (Kupka et al. 1999), as well as molecular lines (Kurucz 1992) and hyperfine transitions (Kurucz 1993), which are tuned to match the line strengths of the Sun and Arcturus (Kirby 2011; Escala et al. 2019).

Synthetic spectra are generated across linearly spaced parameter ranges of  $3500 \leqslant T_{\rm eff}$  (K)  $\leqslant 8000$ ,  $0.0 \leqslant \log(g) \leqslant 5.0$ ,  $-5.0 \leqslant [{\rm Fe/H}] \leqslant 0.0$ , and  $-0.8 \leqslant [\alpha/{\rm Fe}] \leqslant 1.2$ . The microturbulent velocity  $\xi$  used is a linear interpolation between two values out of 0, 1, 2, and 4 km s<sup>-1</sup>, which bracket that given by the relation  $\xi = 2.13 - 0.23 \log(g)$  for red giant stars from Kirby et al. (2009). They cover a wavelength range of 6300–9100 Å, and have a wavelength spacing of 0.02 Å. The synthetic spectra are then interpolated onto the observed wavelength array and smoothed to match the observed spectral resolution,  $\Delta\lambda$ . While the spectral resolution is known to slowly vary both as a function of wavelength and also between masks (Escala et al. 2020a), we keep this fixed at  $\Delta\lambda = 0.45$  to permit the coaddition of stars across different masks (Wojno et al. 2023). 14

## 3.3. Coadding Spectra

As our And XIX spectra have relatively low S/N, it is not possible to derive individual abundance estimates for each target. Instead, we coadd spectra from several member stars in order to calculate average abundance estimates. We initially coadd multiple exposures of the same star on different masks, where these exist; we find for five stars this is sufficient to successfully derive an abundance estimate for the star. <sup>15</sup> For all other stars (including repeat observations of stars on different masks which do not converge when coadded alone), we sort by photometric metallicity and identify groups of  $\sim$ 5 stars to coadd. <sup>16</sup> The pipeline we use to measure coadded abundances is very similar to that which would otherwise be used for

individual stars as described in Kirby et al. (2008) and Escala et al. (2019), with modifications for the coadded spectra as described in Wojno et al. (2020, 2023). We briefly summarize the procedure here.

Each individual 1D spectrum in the coadd is shifted to the rest frame using its LOS velocity, and corrected for telluric absorption features as in Kirby et al. (2008) by dividing the observed spectrum by the scaled template spectrum of a spectrophotometric standard star (Simon & Geha 2007). An initial continuum normalization is performed by fitting a third-order B-spline function with a breakpoint spacing of 100 pixels to continuum regions of the spectrum that are not strongly affected by absorption lines, as defined by Kirby et al. (2008). The normalized spectra for all stars in the coadd group are then combined per Equation (13), with the flux in each pixel,  $f_i$ , weighted by the inverse variance per pixel,  $1/\sigma_i$ , for each of the n spectra in the group. The associated uncertainty for each pixel in the resultant coadded spectrum,  $\sigma_i$ , is therefore given by Equation (14):

$$f_{i} = \frac{\sum_{j}^{n} f_{i,j} / \sigma_{i,j}^{2}}{\sum_{j}^{n} 1 / \sigma_{i,j}^{2}},$$
(13)

$$\sigma_i = \left(\sum_{j=0}^n \frac{1}{\sigma_{i,j}^2}\right)^{-1/2}.$$
 (14)

We subsequently perform an initial fit to the coadded spectrum to determine a first estimate of [Fe/H], during which  $[\alpha/\text{Fe}]$  is held fixed at zero. The synthetic spectrum with which the coadd is compared during this process is itself a coaddition of several synthetic spectra: Each observed spectrum in the group has a corresponding synthetic spectrum, which has  $T_{\rm eff}$ and log(g) fixed at the corresponding photometric values for the associated observed spectrum. When coadding the synthetic spectra, we weight each individual synthetic spectrum by the same inverse variance array as the corresponding observed spectrum in order to account for the differing weight each observed spectrum contributes to the final coadd. In this and all subsequent fitting steps, we use a Levenberg-Marquardt algorithm to minimize the difference between the coadded synthetic and observed spectra, weighting the comparison by the inverse variance of the coadded observed spectrum.

We then perform a fit to the coadded spectrum to derive an initial estimate of  $[\alpha/\text{Fe}]$  in the same manner, during which [Fe/H] is held fixed at the previously determined value. We fit only spectral regions shown to be sensitive to the  $\alpha$  elements of Mg, Si, Ca, and Ti as in Escala et al. (2019) and Kirby et al. (2008); additionally, we mask the infrared Ca II triplet as our synthetic spectra cannot accurately reproduce the shape of these lines (Kirby et al. 2008). Strong TiO features are also not well reproduced by our synthetic spectral grid, but visual inspection of the spectra confirms none of our And XIX member stars have these features. High-resolution studies of other dSphs reveal that abundances of different individual  $\alpha$  elements can vary within stars (see, e.g., Hill et al. 2019; Theler et al. 2020), though these generally follow similar overall trends (Kirby et al. 2020). However, our measurements have

 $<sup>\</sup>overline{\ }^{14}$  Per Escala et al. (2019), assuming a fixed value of  $\Delta\lambda$  with wavelength has no net effect on the derived abundances, and at most increases their associated statistical uncertainties.

<sup>&</sup>lt;sup>15</sup> Defined later in this section.

 $<sup>^{16}</sup>$  Wojno et al. (2020) find negligible differences in the abundances derived for coadd groups sorted by  $T_{\rm eff,phot}$  or [Fe/H]\_phot.

 $<sup>\</sup>overline{^{17}}$  As this is a purely observational shift, we do not apply the heliocentric or *A*-band velocity corrections in this step.

Table 4
Summary of And XIX Coadd Groups

Included Target IDs	[Fe/H] <sub>phot</sub> range	$T_{\rm eff,phot}$ range (K)	$\log(g)_{\text{phot}}$ range (cm s <sup>-2</sup> )
1	Primary Subsample		
a19_00185, 1530, a19_00061, and19_00104	−2.17 to −2.11	4443–4608	0.63-0.96
a19_00134, a19_00095, and19_00022, a19_00069	-2.03 to $-1.99$	4506-4559	0.83-0.96
a19_00115, a19_00098, a19_00098, and19_00047, 1499	-2.06 to $-1.96$	4467–4623	0.77-1.07
and19_00026, and19_00026, and19_00026	-1.95	4511	0.86
and19_00058, a19_00172	-1.95	4399	0.63
1239, and19_00032, a19_00072, 1505, a19_00060	-1.95 to $-1.92$	4403-4511	0.67-0.87
and19_00303, a19_00168, a19_00067, a19_00108, a19_00502	-1.88 to $-1.85$	4411-4704	0.72-1.32
a19_00093, and19_00020	-1.83	4373	0.66
and19_00040, a19_00352, a19_00077, a19_00157, and19_02850	-1.84 to $-1.81$	4328-4683	0.57-1.3
a19_00360, a19_00183, a19_00392, a19_00142, and19_00283	-1.81 to $-1.79$	4576-4621	1.10–1.19
1214, and19_00028, a19_00111, a19_00111	-1.79	4409	0.77
a19_00043, 1540, a19_00078, a19_00443	-1.79 to $-1.77$	4463–4683	0.88-1.33
a19_00343, and19_00265, a19_00428	-1.77 to $-1.73$	4580-4646	1.15–1.26
a19_00411, a19_00431, a19_00149, and19_00043, a19_00087	-1.68 to $-1.61$	4361–4697	0.82-1.41
and19_00134, a19_00418, a19_00348, a19_00546, a19_00182	-1.61 to $-1.46$	4399–4593	0.95-1.35
Low	-probability Subsample		
a19_00377, a19_00302, a19_00425, a19_00414, a19_00384	-1.67 to -1.03	4322–4576	1.08-1.24
C20	Γ Difference Subsample		
and19_00057, a19_00170	-2.06	4499	0.78
and19_00048, a19_00156	-1.85	4539	0.99
a19_00159, a19_00104, a19_00104, a19_00075, a19_00083	-2.14 to $-1.67$	4285-4617	0.62-1.12
a19_00475, a19_00403, and19_00053, a19_00165	-1.59 to $-1.56$	4453-4606	1.02-1.29

Note. A repeated target ID indicates the same star is observed twice on different masks. In addition, some duplicate observations of the same star on different masks are associated with different target IDs depending on when the sets of observations were taken; these are indicated by single values in the subsequent columns.

sufficiently low S/N that even in the coadd groups it is not possible to measure separate abundances for the individual  $\alpha$  elements; the  $[\alpha/\text{Fe}]$  we measure reflects an average of the different contributing elements, and cannot capture these variations.

The continuum of the coadded spectrum is subsequently renormalized using the best-fitting coadded synthetic spectrum. This sequential fitting process and continuum normalization is repeated until the derived [Fe/H] and [ $\alpha$ /Fe] values converge to within tolerances of 0.001 dex. Once continuum refinement is complete, we use the resulting coadded observed spectrum for all subsequent fits.

We then perform an updated fit for [Fe/H], holding  $[\alpha/\text{Fe}]$  fixed at the last best-fit value. We then fit for the ultimate  $[\alpha/\text{Fe}]$  abundance while [Fe/H] is held constant at that value, and subsequently perform a final fit to determine the ultimate [Fe/H] value while holding  $[\alpha/\text{Fe}]$  constant at its ultimate value.

Uncertainties in the fitted abundances are also calculated, along with a reduced  $\chi^2$  statistic for both [Fe/H] and [ $\alpha$ /Fe]. These uncertainties are combined in quadrature with systematic uncertainty floors of 0.101 dex for [Fe/H] and 0.084 dex for [ $\alpha$ /Fe] (derived from M31 data of similar quality and analyzed using the same reduction and abundance pipelines; Gilbert et al. 2019). We define a coadd as successful (i.e., as having a secure abundance determination) if it meets all of the following criteria: (a) the  $\chi^2$  contours for both parameters vary smoothly; (b) the fit parameters are not located at an edge of the spectral synthesis grid; and (c) uncertainties on both [Fe/H] and [ $\alpha$ /Fe] are less than 0.45 (including statistical uncertainties).

We initially identify coadd groups of five targets, starting from those with the lowest photometric metallicity estimates. If a coadd group does not have a secure abundance measurement, we test removing poor-quality or otherwise anomalous spectra from the group and refitting. Should this still not converge, we then add the next closest photometric metallicity target to the coadd group and refit, adjusting subsequent coadd groups accordingly. In total, we obtain 20 unique abundance measurements: 15 in our primary sample, four for which we disagree with C20 on membership based on Na I EWs (our C20  $\Gamma$  difference subsample), and one for our low-probability subsample. Table 2 summarizes the number of targets which contribute to the coadds in each of the different subgroups, and Table 4 presents the properties of the final coadd groups. Coadds with single values for the photometric property range indicate these are comprised solely of duplicate observations of the same star.

### 4. Results

# 4.1. The Abundance Distribution of And XIX

Figure 3 presents the  $\lceil \alpha/\text{Fe} \rceil$ - $\lceil \text{Fe}/\text{H} \rceil$  abundance distribution for all our successful And XIX coadds (tabulated in Table 5). There is a striking decline in  $\lceil \alpha/\text{Fe} \rceil$  as a function of  $\lceil \text{Fe}/\text{H} \rceil$  across the entire metallicity range. The distribution of the C20  $\Gamma$  difference (Section 2.4) and low-probability subsamples largely overlap that of the primary subample of high-confidence And XIX members, and Kolmogorov–Smirnov (K-S) tests also indicate no significant differences in the abundance distributions of these subsamples compared to the primary sample. This indicates these subsamples are likely also comprised predominantly, if not entirely, of genuine And XIX members, and are not strongly contaminated by nonmembers

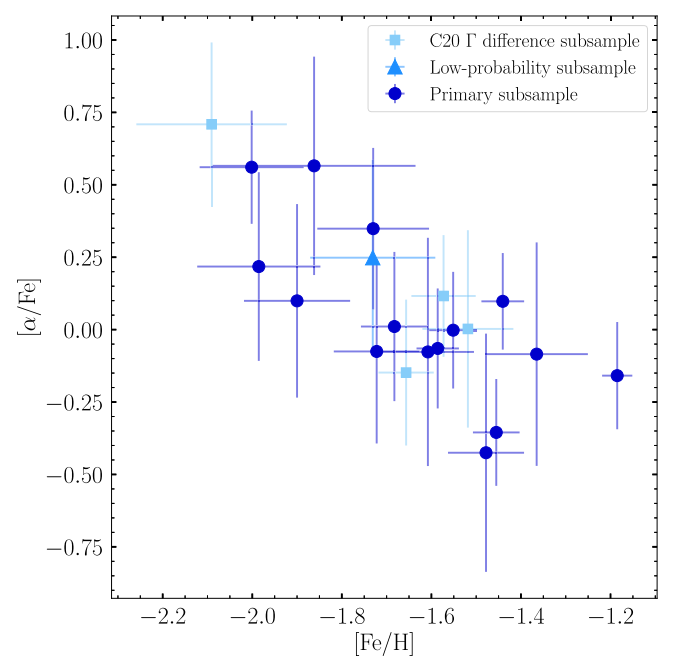


**Figure 3.**  $[\alpha/\text{Fe}]$  vs. [Fe/H] from coadded spectra for And XIX. Circles represent our primary sample of And XIX members. Triangular points represent our "low-probability" subsample, which comprises stars with  $0.1 < P_{\text{tot}} < 0.5$  and which also pass our  $\Gamma/\sigma_{\Gamma}$  cut. Square points represent our "C20  $\Gamma$  difference" subsample, which comprises stars we classify as likely And XIX members but C20 do not based on differing Na I EW thresholds.

Table 5
Elemental Abundances of Coadded Groups

[Fe/H]	$[\alpha/\text{Fe}]$
Primary Subsample	
$-2.00 \pm 0.12$	$0.56 \pm 0.2$
$-1.99 \pm 0.14$	$0.22\pm0.33$
$-1.90 \pm 0.12$	$0.10 \pm 0.33$
$-1.86 \pm 0.23$	$0.57 \pm 0.38$
$-1.73 \pm 0.12$	$0.35\pm0.28$
$-1.72 \pm 0.10$	$-0.08 \pm 0.32$
$-1.68 \pm 0.07$	$0.01 \pm 0.26$
$-1.61 \pm 0.10$	$-0.08 \pm 0.39$
$-1.59 \pm 0.05$	$-0.07 \pm 0.21$
$-1.55 \pm 0.05$	$0.00 \pm 0.20$
$-1.48 \pm 0.08$	$-0.43 \pm 0.41$
$-1.46 \pm 0.05$	$-0.35 \pm 0.18$
$-1.44 \pm 0.05$	$0.10 \pm 0.17$
$-1.36 \pm 0.11$	$-0.08 \pm 0.39$
$-1.19 \pm 0.03$	$-0.16 \pm 0.19$
Low-priority Subsample	
$-1.73 \pm 0.14$	$0.25 \pm 0.34$
C20 Γ Difference Subsample	_
$-2.09 \pm 0.17$	$0.71 \pm 0.28$
$-1.66 \pm 0.06$	$-0.15 \pm 0.25$
$-1.57 \pm 0.07$	$0.12\pm0.21$

from either the M31 or MW halos, both of which have comparatively flatter  $[\alpha/\text{Fe}]$ –[Fe/H] distributions at higher  $[\alpha/\text{Fe}]$  (e.g., Escala et al. 2020a; McKinnon et al. 2023; see also Section 4.3). Accordingly, for the remainder of the analysis, we analyze these collectively (unless otherwise specified).

 $-1.52\pm0.10$ 

We do test varying the isochrone age used to derive the photometric effective temperature and surface gravity for the individual stars that comprise the coadds in order to assess the resulting effects on the derived coadd abundances. However, for isochrones ranging between 10 and 14 Gyr (a range that accounts for  $\sim\!90\%$  of the star formation in And XIX; C22), the resulting derived abundances change negligibly (by a maximum of 0.04 dex in [Fe/H] and 0.03 dex in [ $\alpha$ /Fe], well within the uncertainties on our canonical values). The metallicity range spanned by our coadded measurements is also very similar to that of the photometric metallicities for the underlying sample of individual targets.

The lack of an  $[\alpha/\text{Fe}]$  plateau at low [Fe/H] indicates that most stars in And XIX formed after enough SNIa had occurred to depress  $[\alpha/\text{Fe}]$ . While the oldest (and hence most metalpoor) stars should have been formed prior to the SNIa, our measurements do not extend to sufficiently metal-poor values to identify these stars, and hence the location of the  $[\alpha/\text{Fe}]$  "knee" in And XIX.

Several factors likely contribute to this lack of detection. Low-metallicity stars are inherently relatively rare; in studies using high-resolution spectroscopy (e.g., Theler et al. 2020), the number of stars in low-metallicity [ $\alpha$ /Fe] plateaus is significantly smaller than the number of stars "post-knee". In addition, as low-metallicity stars have shallower spectral lines, they are more difficult to derive confident velocities for in relatively low-S/N observations—including those used in this analysis. As seen in Table 1, we only successfully measure velocities for  $\sim$ 50% of the targets in a given DEIMOS mask; it is plausible that metal-poor stars represent a higher than average fraction of those targets which are "lost" and therefore are not included in our analysis. This may partially explain why  $[\alpha/\text{Fe}]$  "knees" are not observed in similar-luminosity dSphs at metallicity values above [Fe/H] = -2.5 in DEIMOS data (Kirby et al. 2011), but have been detected at lower metallicities in higher-resolution studies (e.g., Lemasle et al. 2014; Theler et al. 2020), which are better able to resolve these shallow lines (at sufficiently high S/N). Finally, the averaging effect introduced by our coaddition of spectra masks the (already inherently narrow) tails of the metallicity distribution, including at the metal-poor end. Deeper observations of And XIX, which allow abundances to be derived for individual stars, would likely help to identify its  $[\alpha/Fe]$  knee—and provide better estimates of the systematic uncertainty associated with our abundance measurements, through duplicate target observations.

We also do not see an  $[\alpha/\text{Fe}]$  plateau at high metallicity. Such plateaus can occur when star formation is constant for a sufficiently long duration that the ratio of Type Ia to Type II SNe becomes constant, with a resulting equilibrium in the production of  $\alpha$  elements and iron (Kirby et al. 2011). Alternatively, they can also form in systems that have very rapid repeated bursts of star formation, which mimics the effects of constant star formation (Revaz et al. 2009). However, these plateaus are typically only observed in more massive systems with extended star formation such that they reach metallicities above [Fe/H]  $\gtrsim -1.2$  (Kirby et al. 2011). Given similar-luminosity systems like Sex do not show this plateau, and the metallicity distribution of And XIX does not extend to very metal-rich values, the lack of a high-metallicity plateau is expected. This also aligns with the star formation history (SFH) of And XIX presented by C22, which indicates that two distinct

 $0.00\pm0.34$ 

bursts of star formation formed >90% of the stars in And XIX, without the extended star formation or rapid repeated bursts necessary for  $[\alpha/Fe]$  equilibrium to be reached.

### 4.2. Comparison with Literature Metallicities

While C20 do not derive  $\alpha$ -element abundances for And XIX, they do present [Fe/H] estimates derived from calibrations of the equivalent width (EW) of the near-infrared calcium II triplet (CaT). As we mask the CaT during our usual fitting process due to strong non-LTE effects which our synthetic spectra cannot accurately describe, this effectively provides an entirely independent [Fe/H] estimate.

Their metallicity distribution, derived for individual And XIX member stars with S/N > 5 Å^{-1}, has a mean [Fe/H] =  $-1.8 \pm 0.1$  dex and a dispersion of  $\sim\!0.5$  dex (after accounting for uncertainties in the individual measurements, which themselves are on the order of 0.5 dex). In contrast, the metallicity distribution we derive from our full sample of coadded measurements has a mean [Fe/H] of  $-1.50 \pm 0.02$  dex, and a dispersion, accounting for the individual measurement uncertainties, of  $\sim\!0.2$  dex. Given that we have significantly fewer data points, each of which combines data from multiple stars, it is no surprise the width of our distribution is substantially narrower.

Less clear is the source of the  $\sim 3\sigma$  higher mean metallicity we derive, as there are several factors which could potentially contribute to this difference. Most likely is that this is due to the two different techniques used to derive the metallicities. In order to test this effect, we also calculate [Fe/H] values for stars we consider potential And XIX members using the same CaT equivalent calibration as in C20. To do so, we first fit a Voigt profile to the 8542 and 8662 Å Ca II lines in each spectrum using the package PHEW (Núñez et al. 2022), and sum the associated EW for each. We then use the calibrations presented in Starkenburg et al. (2010) based on the absolute magnitude  $M_V$  (which we convert from the observed V-band magnitude assuming a distance modulus of 24.57 per Section 2.2) to derive a [Fe/H] value for each star.

Because the S/Ns of the spectra are low, we find that we can only reliably fit the CaT lines, and therefore derive a useful metallicity, for 18 stars. The mean of this distribution is  $-1.81\pm0.06$ , entirely consistent with that derived by C20. This suggests that the different underlying sample of member stars and data-reduction methods we use compared to C20 do not significantly affect the derived metallicities, but that the different techniques used to derive the metallicity do have an impact.

In particular, we point out that the Starkenburg et al. (2010) calibration is derived using model spectra with  $\lceil \alpha/\text{Fe} \rceil \geqslant 0$ . Per Figure 3, this is only true for seven of our 20 coadds, predominantly those which are metal-poor, with  $\lceil \text{Fe}/\text{H} \rceil \lesssim -1.7$ . In contrast, the majority of our measurements—particularly those which are more metal-rich—have  $\lceil \alpha/\text{Fe} \rceil < 0$ . This means that a  $\lceil \text{Fe}/\text{H} \rceil$  estimate derived from the CaT calibration will be underestimated for these (metal-rich) stars. Indeed, for a similar CaT calibration, Da Costa (2016) finds that a reduction in  $\lceil \alpha/\text{Fe} \rceil$  by 0.5 dex will result in  $\lceil \text{Fe}/\text{H} \rceil$  values derived from CaT abundances being underestimated by  $\sim 0.15$  dex. Since our data span an even larger  $\lceil \alpha/\text{Fe} \rceil$  range than this, we expect the CaT metallicities to be similarly affected, and we suggest this is largely why the average

metallicity we derive for And XIX using spectral synthesis is higher than that derived using the CaT.

Another potential contributor to the difference in mean metallicities is that our abundances are derived for coadded spectra of multiple stars. As discussed in Section 4.1, the coadded measurements inherently trend toward the mean of the underlying data, and therefore mask any narrow metal-poor tail in the distribution. In contrast, deriving metallicities for individual stars allows any metal-poor tail to be captured, resulting in a lower overall mean metallicity. To distinguish between this effect and that of the different calibration methods described above would require both the CaT calibration and spectral synthesis to be applied to identical spectra. It is nominally possible to apply the CaT calibration to the coadded spectra used for spectral synthesis; however, this would require assigning a singular V-band magnitude to a coadd of multiple stars that span a range of almost 1.5 magnitudes in brightness. This is neither particularly physically meaningful nor likely reflective of the coadded spectrum used to perform the measurements given the varying contributions of each individual star in the coadd at any given pixel. Deeper observations of And XIX, which allow abundances to be derived for individual stars, would eliminate any such magnitude biases in the CaT calibration associated with coaddition and allow for a 1:1 comparison between the abundances derived using the two methods.

#### 4.3. And XIX in Context

We compare the abundances we derive for And XIX to other dSph satellites of the MW and M31 (left and right panels of Figure 4, respectively) also derived from DEIMOS data using similar techniques. Starred points with black outlines indicate coadded abundances for our full sample; other shapes indicate abundances for other satellites taken from the literature, with all points color-coded by the V-band luminosity of the satellite (all taken from McConnachie 2012, for consistency). All MW satellite abundances are taken from Kirby et al. (2010), and are measured for individual stars. Those abundances are provided for individual  $\alpha$  elements (one or more of Mg, Si, Ti, and Ca); we calculate an "overall"  $\alpha$ -element abundance for comparison by taking the average of all available values for a given star, weighted by the inverse square of the individual element uncertainties. For clarity, in the figure we only plot measurements where the  $[\alpha/Fe]$  uncertainty is <0.5 dex. Abundances for all M31 satellites are taken from Wojno et al. (2020), measured for a combination of individual stars and coadded spectra using the same method as this paper. In addition, abundances obtained from deep spectra of individual stars in select M31 satellites are included where available: We source measurements for And I, III, V, VII, and X from Kirby et al. (2020), taking the bulk [ $\alpha$ /Fe] even when measurements of individual  $\alpha$  elements are available. We do not include individual stellar abundances from Vargas et al. (2014) as Kirby et al. (2020) analyze an overlapping sample of stars with deeper data, and identify a systematic [Fe/H] difference of 0.25 dex between their measurements. Given the method used by Kirby et al. (2020) is more similar to ours than that of Vargas et al. (2014), we preferentially take the former.

The abundances we measure for And XIX are comparable with those of similar-luminosity satellites, both in terms of overall  $[\alpha/\text{Fe}]$  and [Fe/H] abundances, and their associated dispersions. We confirm this by performing 2D K-S tests,

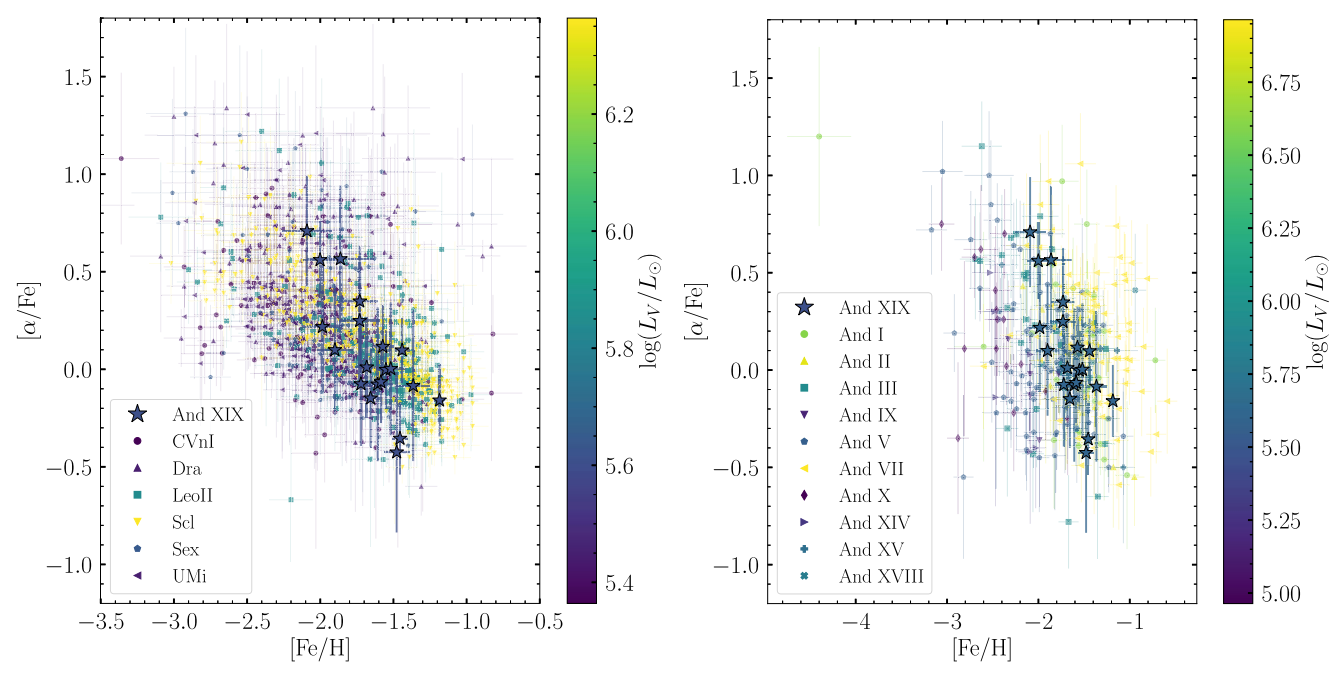


Figure 4. Literature values of  $[\alpha/\text{Fe}]$  vs. [Fe/H] for various MW (left) and M31 (right) dSph satellites, color-coded by log-luminosity (see text for full source list). Our codded And XIX measurements are indicated by starred points; these have a similar distribution to those of other dSphs.

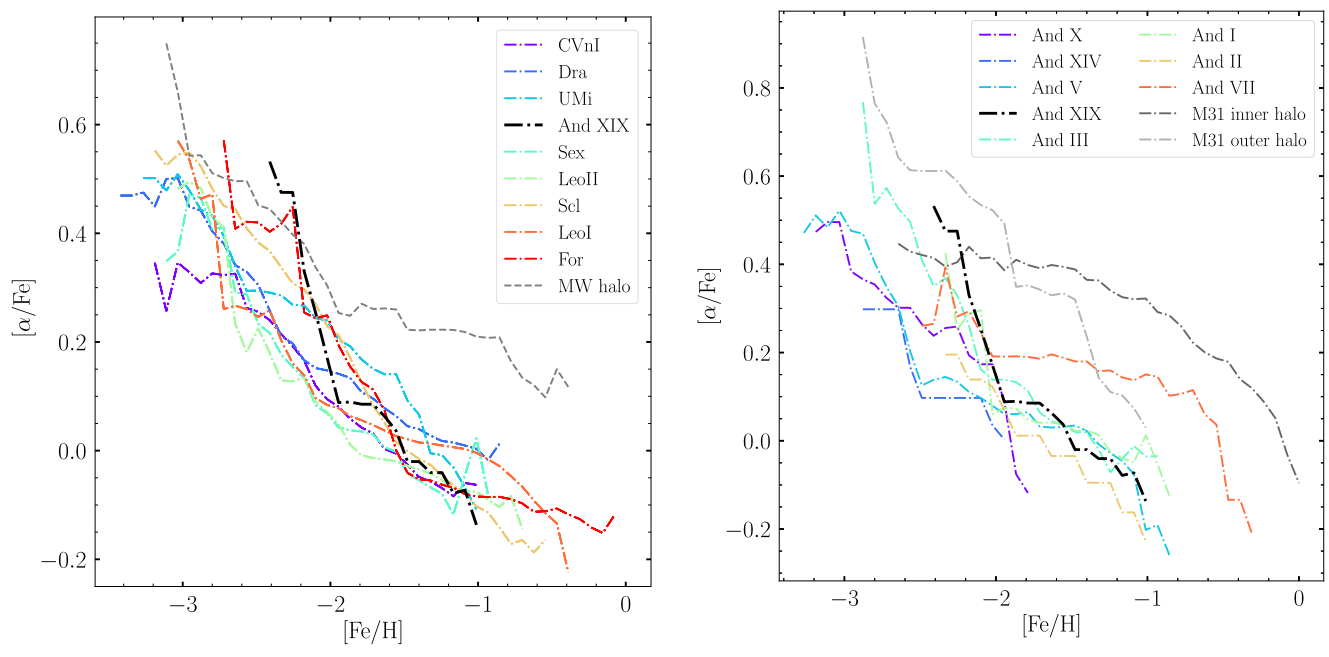


Figure 5. Moving averages of  $[\alpha/\text{Fe}]$  as a function of [Fe/H] for various MW (left) and M31 (right) dSph satellites (see text for full source list). Galaxies are listed from least to most luminous. A solid black line indicates our And XIX measurements. Dashed gray lines indicate average values for the MW and M31 (inner and outer, defined as within and beyond 30 kpc, respectively) halos in their respective panels. And XIX displays a very similar trend to that seen in most other dSphs.

comparing the  $[\alpha/\text{Fe}]$ –[Fe/H] distribution of And XIX to combined distributions of the MW and other M31 satellites; in both cases, there are no significant differences in the abundance distributions. In Figure 4, this is clearest in the comparison with other M31 satellites, but is true also in the comparison to MW satellites; here, the more numerous measurements for satellites of higher and lower luminosities (only Sex has a very similar luminosity to And XIX) wash out the trend. To make this clearer, in Figure 5 we present the moving average of the  $[\alpha/\text{Fe}]$  abundances as a function of [Fe/H] for the MW (left) and M31 (right) satellites, respectively. This is calculated by

taking the average of  $[\alpha/\text{Fe}]$  measurements, weighted by the inverse square of the measurement uncertainties, in moving windows of 0.5 dex in [Fe/H]; we exclude bins where <5 [ $\alpha/$ Fe] measurements contribute to the average. This means some M31 satellites with very few abundance measurements are excluded from the plot entirely, as are the tails of the [Fe/H] distribution that include very few measurements. In addition, in these plots we show in gray the average [ $\alpha/\text{Fe}$ ] versus [Fe/H] trend for the MW halo (McKinnon et al. 2023) and the inner ( $<30\,\text{kpc}$ ; Escala et al. 2020b; Wojno et al. 2023) and outer ( $>30\,\text{kpc}$ ; Wojno et al. 2023) halo of M31. We choose these

reference samples as they are all derived using very similar methods on similar DEIMOS data, which should minimize any potential systematic differences.

Qualitatively, the decrease in  $[\alpha/\text{Fe}]$  as a function of [Fe/H]for And XIX is very similar to that seen in other dSphs, and the outer halo of M31, which Wojno et al. (2023) suggest is likely comprised of debris accreted from several such small satellites. While it appears that the M31 satellites And V and X have significantly lower  $[\alpha/\text{Fe}]$  abundances than their MW counterparts at the metal-rich end of their distributions, this appears likely to be at least partially an artifact due to the low number of stars in the surrounding bins for these two galaxies, compared to that of their MW counterparts at the same metallicity. This means that a handful of low- $\alpha$  stars in this bin, well within the overall abundance scatter of the galaxy, can have an outsized effect on the running mean reported in Figure 5. We also note there is no clear evidence of metal-poor plateaus for any galaxies in Figure 5. As discussed in Section 4.1, this is due to the underlying limitations of the chosen comparison samples (which are shared with our And XIX data)—higher-resolution studies of several MW satellites do find high  $[\alpha/Fe]$  plateaus at very low metallicities (e.g., Lemasle et al. 2014; Hill et al. 2019; Theler et al. 2020).

The slope of the  $\lceil \alpha/\text{Fe} \rceil$ - $\lceil \text{Fe}/\text{H} \rceil$  trend, as seen in Figure 5, is linked to the chemical evolution history and mass of a system. The shallow gravitational potential well of low-mass systems facilitates gas loss due to stellar feedback (Dekel & Silk 1986), which not only suppresses the increase of  $\lceil \text{Fe}/\text{H} \rceil$  in the system, but also results in a lower overall SFR, allowing the rate of SNIa to dominate that of core-collapse SNe and producing a steeper  $\lceil \alpha/\text{Fe} \rceil$  slope (Kirby et al. 2020). In contrast, more massive systems better retain their (enriched) gas, allowing for a higher rate of star formation over an extended period. This not only results in a comparatively higher rate of Type II SNe, but also increases the overall  $\lceil \text{Fe}/\text{H} \rceil$  of the system, both of which produce a shallower  $\lceil \alpha/\text{Fe} \rceil$  gradient (Kirby et al. 2020).

This is clearly seen in the inner halo of M31, which likely comprises debris from more massive satellites than those which survive today (Escala et al. 2020a; Kirby et al. 2020), and which has a correspondingly shallower slope in Figure 5. The slope of the MW halo in Figure 5 is also somewhat shallower, particularly at the metal-rich end, but is comparatively steep at the metal-poor end. This is because the McKinnon et al. (2023) sample includes MW halo stars with a variety of origins. The metal-rich end is dominated by "in-situ" halo stars heated from the MW disk and debris from Gaia-Sausage-Enceladus—which, being relatively massive, has a shallow  $[\alpha/\text{Fe}]$  gradient (e.g., Hasselquist et al. 2021)—while the metal-poor end is comprised of debris from smaller satellites, with accordingly shallower  $[\alpha/\text{Fe}]$  gradients (e.g., Naidu et al. 2020).

It is also worth noting the diversity of  $[\alpha/\text{Fe}]$ –[Fe/H] slopes in M31 satellites compared to those in the MW. While the lower-mass MW satellites (i.e., Sex and below) largely overlap in this space—with this similarly being observed in higher-resolution studies (e.g., Fernandes et al. 2023)—the  $[\alpha/\text{Fe}]$ –[Fe/H] locus of M31 satellites varies significantly. To quantify this, we measure the slope  $d[\alpha/\text{Fe}]/d[\text{Fe}/\text{H}]$  using the method described in Section 7 of Wojno et al. (2020). That work shows such a slope derived from coadded measurements accurately reflects that derived from abundance measurements of individual stars. In particular, we parameterize the trend with an angle  $\theta$ , and the perpendicular distance of the line from the

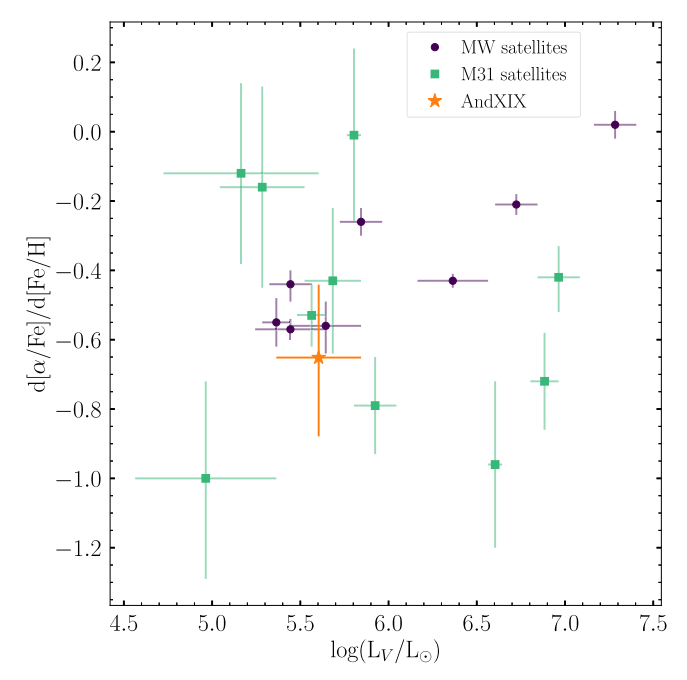


**Figure 6.**  $d[\alpha/\text{Fe}]/d[\text{Fe}/\text{H}]$  slope as a function of log-luminosity for Local Group dSphs (see text for full source list). Steeper (i.e., more negative) slopes indicate a stronger contribution of SNIa to the chemical evolution of the galaxy. Purple circles indicate MW dSphs and green squares indicate M31 dSphs; the starred orange point represents our measurement for And XIX.

origin  $b_{\perp}$  per Equation (15):

$$[\alpha/\text{Fe}] = [\text{Fe/H}]\tan(\theta) + \frac{b_{\perp}}{\cos(\theta)}.$$
 (15)

This avoids the preference for shallow slopes when the  $d[\alpha/\text{Fe}]/d[\text{Fe}/\text{H}]$  slope is fit directly with a flat prior (Hogg et al. 2010). We sample the posterior distribution of the parameters (both with flat priors) using the Markov Chain Monte Carlo ensemble sampler EMCEE (Foreman-Mackey et al. 2013), taking the 50th percentile of the resulting distribution as our measured value, and the 16th and 84th percentiles as the associated uncertainties. We then back-calculate the associated slope as  $d[\alpha/\text{Fe}]/d[\text{Fe}/\text{H}] = \tan(\theta)$ . A slope of -1 would imply constant  $[\alpha/\text{H}]$ , i.e., enrichment solely by SNIa with no contribution from core-collapse SNe (Kirby et al. 2020).

We measure a  $d[\alpha/\text{Fe}]/d[\text{Fe/H}]$  slope of  $-0.65^{+0.21}_{-0.23}$  for And XIX, and compare this to literature measurements of this slope reported for other dSphs using the same method in Figure 6. Measurements for MW dSphs are taken from Kirby et al. (2020). For M31 satellites, we preferentially take measurements from Kirby et al. (2020), as these are derived from larger samples of individual stellar abundances; the remaining M31 satellites (And II, IX, XIV, XV, and XVIII) are sourced from Wojno et al. (2020).

The  $[\alpha/\text{Fe}]$ –[Fe/H] gradient in And XIX is relatively steep, and is consistent with that of similar-luminosity dSphs, such as Sex. This implies a similar chemical evolution history for these galaxies, which aligns with the similar SFHs observed. For example, the SFH of Sex indicates that it formed the majority of its stars in the first 1–2 Gyr after the Big Bang, with minimal to no star formation more recently than 11 Gyr ago (Bettinelli et al. 2018; Lee et al. 2009); this is very similar to the SFH of And XIX, which also experienced the majority of its star formation prior to reionization, and has no star formation within the last 8–10 Gyr (C22). In general, however, there is

significantly more scatter in this plane for M31 satellites compared to MW satellites, which clearly trend toward shallower slopes with increasing luminosity. This is likely linked to global differences in the SFHs, and therefore chemical evolution, of M31 and MW satellites. In particular, Weisz et al. (2019) find that the time at which star formation is quenched—with more recent quenching times resulting in higher metallicities and shallower [ $\alpha$ /Fe]–[Fe/H] slopes—is effectively independent of luminosity for M31 satellites, but is strongly correlated with luminosity for MW satellites (e.g., Brown et al. 2014; Weisz et al. 2015).

## 5. Discussion: The Origin of And XIX

Multiple different scenarios have been proposed to explain the diffuse appearance of And XIX. Here, we discuss what our abundance measurements, in conjunction with its other observed properties, imply for its formation.

### 5.1. Tidal Interactions

In this scenario, And XIX experienced a strong tidal interaction with a much larger system (the most likely candidate being M31), which resulted in its dark and baryonic matter being redistributed outward—and/or stripped—to produce the diffuse system observed today. Even before considering abundances, And XIX possesses numerous characteristics suggestive of it having experienced tidal interactions. These include distorted outer isophotes (McConnachie et al. 2008), a mild  $(-2.1 \pm 1.7 \,\mathrm{km \, s^{-1} \, kpc^{-1}})$  velocity gradient and spatially varying velocity dispersion (C20), and its vicinity to other low-surface-density features. In particular, it is near what Ibata et al. (2007) first identify as diffuse structure aligned with the major axis of M31, and which extended data in McConnachie et al. (2008, 2018) show as a broader complex of substructure that extends to the northeast of And XIX, though no clear association between And XIX and these diffuse structures has been proven. In addition, the nominal association of And XIX with a nearby stream-like feature to the southwest is debated given an  $\sim$ 0.4 dex metallicity difference between the systems (C20).

If And XIX has experienced significant tidal stripping as a result of interactions, we expect it to have a mean metallicity higher than that predicted by the present-day stellar massmetallicity relation for dSphs (Kirby et al. 2013). The previous measurement of And XIX's metallicity by C20 placed it approximately  $2\sigma$  below this relation, making this unlikely; however, as per Section 4.2, our mean metallicity is  $\sim$ 0.6 dex higher. We thus compare our updated metallicity to the Kirby et al. (2013) relation in Figure 7. The orange star represents our new measurement, calculated as the average of all coadd [Fe/H] measurements, weighted by the inverse square of their uncertainties; the gray star shows the previous measurement from C20. Our new [Fe/H] measurement now places And XIX approximately  $2\sigma$  above the mass–metallicity relation.

If And XIX was originally on the mass–metallicity relation, this implies it had a luminosity of  $\sim 4.5 \times 10^6 L_{\odot}$ ; assuming a stellar mass-to-light ratio of  $1.6 M_{\odot}/L_{\odot}$ —the average value for dSphs measured by Woo et al. (2008)—implies an initial stellar mass of  $\sim 7.2 \times 10^6 M_{\odot}$ . This is a factor of 10 higher than And XIX's current stellar mass assuming the same M/L ratio ( $\sim 6.4 \times 10^5 M_{\odot}$ ), requiring a loss of  $\sim 90\%$  of its initial stellar mass. Even if And XIX was originally at the upper envelope of

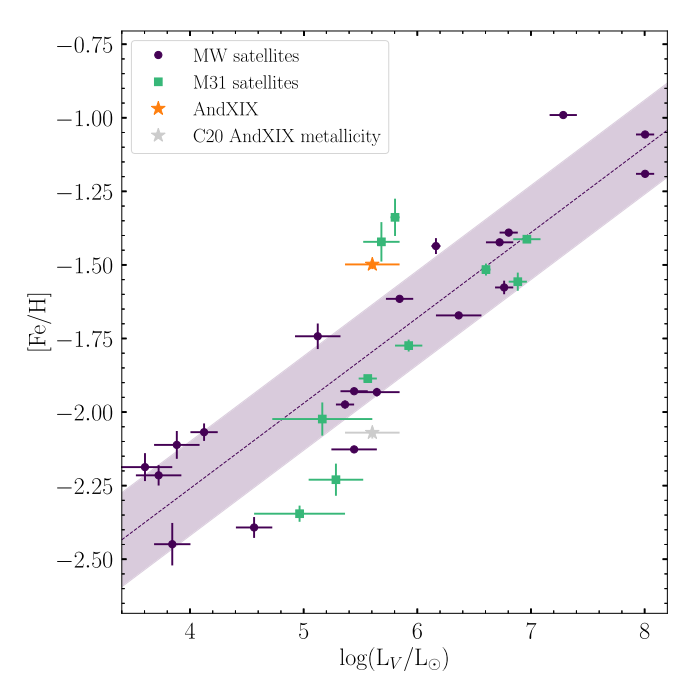


Figure 7. Luminosity–metallicity relation for Local Group dSphs. The purple dashed line and shaded regions represent the mass–metallicity relation and its associated rms scatter of 0.16 dex from Kirby et al. (2013). Purple circles indicate MW dSphs and green squares indicate M31 dSphs; points without [Fe/H] error bars have sufficiently small ranges (due to being averages of many data points) that these are not visible. The gray starred point represents the previous CaT-based And XIX metallicity from C20; our new measurement (orange starred point) is  $\sim\!0.6$  dex more metal-rich (see Section 4.2), placing it  $\sim\!2\sigma$  above the mass–metallicity relation.

the  $1\sigma$  scatter within the mass–metallicity relation, this still implies a minimum loss of  $\sim$ 65% of its initial stellar mass. Strong tidal interactions are required for such significant stripping.

Simulations by Peñarrubia et al. (2008a, 2008b) support this picture. They find a loss of 90% of a satellite galaxy's stellar mass can maintain (or increase) its half-light radius—consistent with the large radius of And XIX—while leaving its internal kinematics largely unchanged. In addition, they find tidal stripping tends to increase the *total* mass-to-light ratio; this is consistent with the unusually large total M/L ratio measured for And XIX by C20.

If And XIX was originally  ${\sim}10\times$  more massive than its current luminosity suggests, this might allow it to initially retain more gas than satellites with similar present-day luminosities, and thus reach a higher metallicity. This would explain the mild horizontal shift seen in Figure 5 of its  $[\alpha/\text{Fe}]$ –[Fe/H] trend toward higher [Fe/H] values relative to the currently similar-mass satellites Sex and And V, closer to that of, for example, And I and Leo I, which have stellar masses closer to that of And XIX's nominal original mass assuming it began on the mass–metallicity relation. This is particularly clear at  $[\alpha/\text{Fe}]$  values >0.1 (i.e., [Fe/H] values <-2), where And XIX is up to 0.5 dex higher in metallicity than the satellites most similar to its current luminosity.

The steep  $d[\alpha/\text{Fe}]/d[\text{Fe}/\text{H}]$  gradient we observe for And XIX is not inconsistent with this picture—an early tidal interaction that strips gas from And XIX could mimic the effect of gas loss via internal mechanisms in lower-mass galaxies, producing a similarly steep  $[\alpha/\text{Fe}]$ —[Fe/H] gradient. The SFH of And XIX, which indicates it quenched  $\sim$ 10 Gyr ago and has

 Table 6

 Masses, Positions, and Kinematics Used for And XIX Orbital Modeling

Parameter	Value	Source
M31 mass	$1.2 \times 10^{12}  M_{\odot}$	Van Der Marel et al. (2012)
And XIX mass	$1.1 \times 10^8~M_{\odot}$	C20
MW-M31 distance	770 kpc	Karachentsev & Kashibadze (2006)
MW-And XIX distance	821 kpc	Conn et al. (2012)
And XIX-M31 distance	115 kpc	Conn et al. (2012)
$V_{\rm LOS}$ , M31	$-301 \text{ km s}^{-1}$	Karachentsev & Kashibadze (2006)
$V_{\rm LOS}$ , And XIX	$-110  \mathrm{km  s^{-1}}$	C20

not experienced any recent star formation (C22), is consistent with such a picture.

Overall, we consider that tidal interactions are a likely candidate for the formation of And XIX. If those tidal interactions were with M31, this may indicate And XIX is on a highly radial orbit, since simulations suggest tidal interaction mechanisms are most effective when satellites are on strongly radial orbits and thus experience close interactions (e.g., Macciò et al. 2020; Moreno et al. 2022). This is the case for the similarly diffuse Ant II, which has a close orbital pericentre of  $38.6^{+7.2}_{-5.8}$  kpc around the MW, and is thought to be the product of tidal interactions (Ji et al. 2021). Proper-motion measurements are necessary to accurately model the orbit of And XIX and confirm if tidal interactions with M31 are a plausible formation mechanism. If the proper motions of And XIX are aligned with its velocity gradient (which, per C20, is aligned with the major axis of the galaxy), this would be further indicative of tidal interactions as its origin; a similar alignment of these three features is observed in Ant II (Ji et al. 2021).

#### 5.1.1. Orbital Modeling

Motivated by the above scenario, we perform a preliminary test of whether And XIX is likely to have experienced close tidal interactions with M31. We use the framework described in Kvasova et al. (2024; see their Appendices B and C for details), and investigate the effects of different tangential velocities  $v_{\tau}$  of And XIX relative to M31 on its possible orbit. For simplicity, we consider only the two-body problem (And XIX-M31), assuming a point-like, static potential for both galaxies. Table 6 presents the parameters we use for the models.

Figure 8 shows different possible orbits of And XIX around M31 in the two-body scenario; the orbits are projected onto an x-y plane along the LOS from the observer to M31 such that a positive radial velocity is to the right (away from the MW), and a positive tangential velocity  $v_{\tau}$  is downwards (i.e., along the negative y-axis). Both the radial and tangential velocities are relative to M31's systemic motion. The system is closed (i.e., And XIX is bound to M31) while  $|v_{\tau}| < 231.3 \,\mathrm{km \, s^{-1}}$ ; And XIX is currently at pericentre if  $v_{\tau} = -109.7 \,\mathrm{km \, s^{-1}}$ .

We find there are broadly three qualitatively different families of orbits for And XIX that can reproduce the observed data. The first are those where it has a tangential velocity  $v_{\tau} < -109.7 \, \mathrm{km \, s^{-1}}$  (top row of Figure 8); in this scenario, it has experienced at least one previous pericentric passage around M31 on the order of several billion years ago (and has not yet reached pericentre again). These orbits all have fairly distant pericentres, comparable to And XIX's current distance from M31 ( $\sim$ 115 kpc). This aligns with the scenario predicted for And XIX by Watkins et al. (2013), who suggest an orbital

pericentre for And XIX of  $112 \pm 12 \, \mathrm{km \, s^{-1}}$  based on the timing argument. However, these orbits are not the strongly radial ones necessary to substantially tidally disrupt the stellar component of And XIX.

The second category of orbits correspond to  $-110 \lesssim v_{\tau} \lesssim 0 \, \mathrm{km \, s^{-1}}$  (second row of Figure 8). In this family of orbits, And XIX is on a mostly circular orbit, with broadly similar peri- and apocentric distances ( $\sim 50-150 \, \mathrm{kpc}$ ), and has recently experienced a pericentric passage around M31. These are again too distant to substantially tidally perturb the central regions of And XIX.

The third category of orbits corresponds to  $v_{\tau} \gtrsim 0 \, \mathrm{km \, s^{-1}}$  (bottom row of Figure 8). These orbits have fairly long periods, with And XIX only experiencing a pericentric passage relatively recently (within the past  $\sim$ Gyr). They are, however, strongly radial orbits, with pericentric distances within  $\sim$ 50 kpc of M31—certainly strong enough to tidally disturb And XIX and produce the diffuse galaxy we see today.

Among all the range of orbits discussed above, the MW has relatively little effect. While some orbits appear to pass close to the MW in the top row of Figure 8, these both (a) do not account for the increased distance between the MW and M31 in the past (since this is a two-body-only model), and (b) in some cases correspond to sufficiently long-period orbits that such passages would actually occur in the future, as the left column of Figure 8 plots one full orbital period, regardless of whether sufficient time has passed for And XIX to actually complete such an orbit.

The above modeling suggests that there are several reasonable orbital solutions—with  $v_{\tau} \gtrsim 0 \, \mathrm{km \, s^{-1}}$ —where And XIX has passed close enough to M31 to have experienced strong tidal interactions within the past  $\sim$ Gyr. However, as sufficient time must have passed since a close interaction for And XIX to expand and return to virial equilibrium to produce its current observed properties, this suggests orbits where this interaction is very recent (corresponding to the largest  $v_{\tau}$ ) are implausible. Our models also suggest it is unlikely that a singular interaction has led to both the quenching and tidal expansion of And XIX, due to the very different timescales of these events ( $\gtrsim$ 8 Gyr ago and  $\lesssim$ 1 Gyr ago, respectively).

These are, however, very simple models. More sophisticated modeling—beyond the scope of this paper, but which includes, for example, dynamical friction (not present in these models), a more realistic shape for M31's gravitational potential (rather than the point-like one used in these models), the growth of M31's dark matter halo over time (fixed at its current mass in these models, which is a particularly bad assumption at ancient times concurrent with And XIX's SF quenching), and the effect of massive satellites like M33 and the progenitor of M31's Giant Stellar Stream on M31's gravitational potential, which

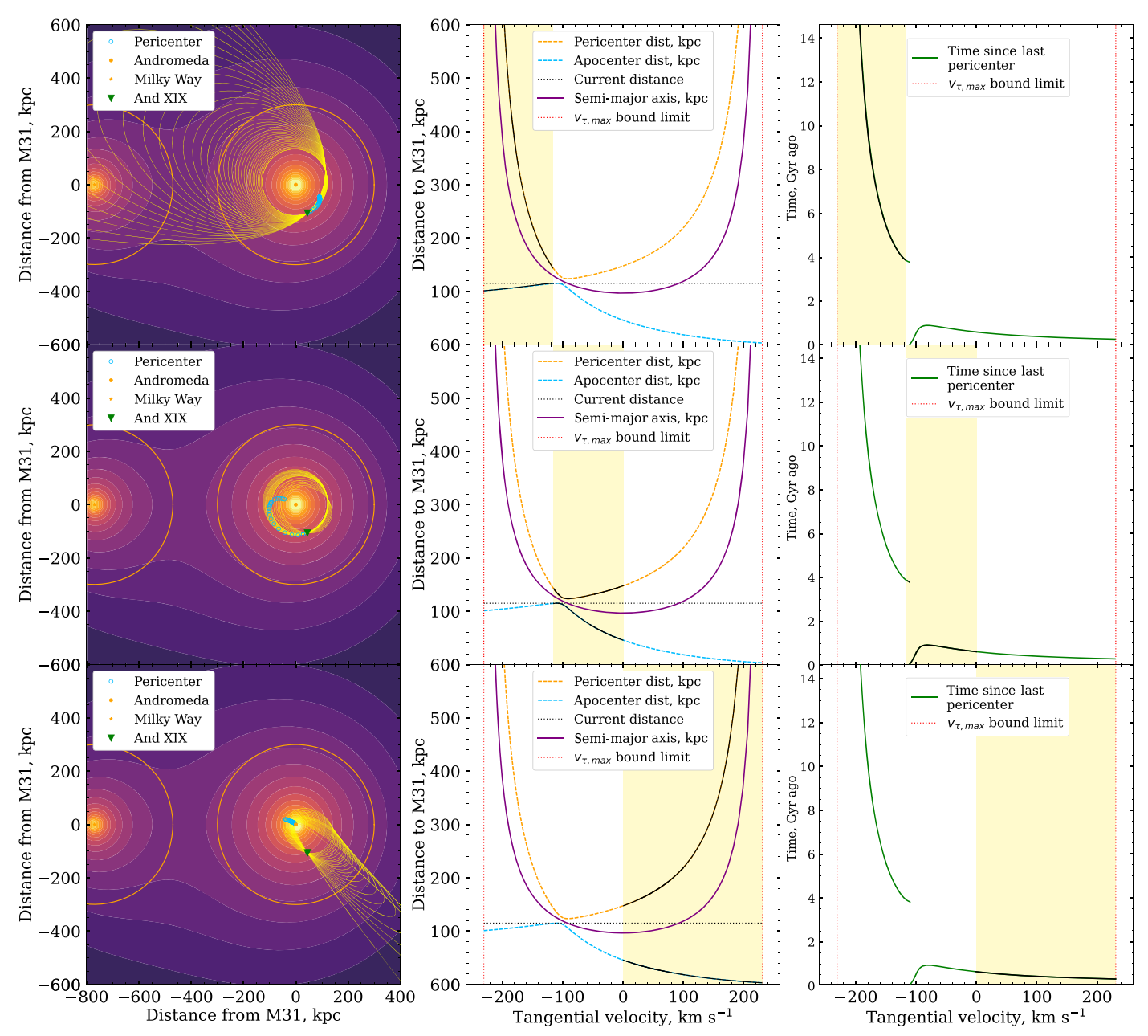


Figure 8. Left column: possible orbits for And XIX around M31 in a two-body framework for different relative tangential velocities  $v_\tau$ ; the tangential velocity is positive along the negative y-axis. Each yellow line shows a singular orbit (i.e., apocentre to apocentre) for a given value of  $v_\tau$  which passes through And XIX's current position, sampled from the yellow shaded region in the right column. The background contour plot illustrates the equipotential surfaces for the MW (for reference only) and M31, with orange circles indicating their virial surfaces (at 300 kpc). Green triangles indicate And XIX's current position. Blue circles indicate the pericentre associated with each orbit. Different rows indicate different ranges of orbits associated with different ranges of tangential velocities:  $v_\tau < 109 \text{ km s}^{-1}$  (top),  $-109 < v_\tau$  km s<sup>-1</sup> < 0 (middle), and  $v_\tau > 0 \text{ km s}^{-1}$  (bottom). Middle column: orbital properties of And XIX associated with different tangential velocities. The horizontal dotted black line indicates And XIX's current distance from M31; the vertical red dotted lines correspond to  $|v_\tau| = 231 \text{ km s}^{-1}$  (the limit between which And XIX is bound to M31). Yellow dashed and dotted lines indicate the pericentric and apocentric distances from M31; these are shown as solid black lines for the range of tangential velocities plotted in the corresponding row. The purple line indicates the semimajor axis of the orbit. Right column: time since And XIX's last pericentric passage as a function of tangential velocity (green), shown as a solid black line for the range of tangential velocities plotted in the corresponding row. Both strongly radial and relatively circular orbits are possible for And XIX; these can be grouped into three qualitatively different scenarios, differentiated by the assumed tangential velocity (Section 5.1.1).

can subsequently affect the orbits of its satellites (similarly to how to the LMC affects the gravitational potential of the MW and its satellites; e.g., Gómez et al. 2015)—is critical in order to test whether there are truly orbits which can naturally explain all of And XIX's properties.

Given all of the above uncertainties, it is quite possible And XIX is not on a long-term bound orbit around M31, and therefore has not closely interacted with it in the past. However,

even if future proper-motion measurements reveal And XIX is on an orbit such that it has not closely interacted with M31, this may not rule out tidal interactions as a formation mechanism. It is also possible And XIX could have tidally interacted with another galaxy  $\sim 8-10$  Gyr ago (e.g., the progenitor of M31's last, likely major, merger; Hammer et al. 2018). More detailed simulations of the entire M31 system would be required to confirm or deny such a scenario.

#### 5.2. Bursty Star Formation

In this scenario, feedback from vigorous star formation in And XIX deposited energy back into its dark and baryonic matter, causing it to expand into the diffuse system seen today (e.g., Di Cintio et al. 2017; Read et al. 2019). However, as discussed in C22, the purely ancient SFH of And XIX does not align with this potential formation mechanism; Read et al. (2019) find extended star formation, to within the last ~6 Gyr, is necessary to significantly impact the central dark matter density of a galaxy, inconsistent with And XIX's quenching  $\sim 10$  Gyr ago. In addition, Chan et al. (2018) find the effects of stellar feedback on dark and baryonic matter are strongest in galaxies with stellar masses  $M_* \sim 10^8 M_{\odot}$ . This is 3 orders of magnitude larger than And XIX's current stellar mass ( $\sim 6 \times 10^5 M_{\odot}$ ). Even if And XIX has undergone significant tidal stripping, as described in Section 5.1, its nominal original mass based on the current-day massmetallicity relation,  $\sim 7 \times 10^6 M_{\odot}$ , is still well below the regime where bursty star formation is thought to have a significant effect. The steep  $[\alpha/Fe]$  gradient we measure for And XIX is also inconsistent with extended bursty star formation as a formation mechanism. In this scenario, shallow  $[\alpha/Fe]$  slopes are expected, due initially to the dominance of Type II SNe during the vigorous star formation bursts, and subsequently to the reaching of equilibria between Type II and Type Ia SNe over the extended duration of the repeated bursts (Revaz et al. 2009). We can therefore confidently rule out extended, bursty star formation as the formation mechanism of And XIX.

## 5.3. Mergers

There are several different merger-related channels which could nominally result in the formation of And XIX, each of which will imprint different signatures on its properties.

In the high-velocity collision scenario, two relatively gasrich dwarf galaxies collide  $\gtrsim 10\,\mathrm{Gyr}$  ago at a relatively high velocity ( $\sim 300\,\mathrm{km\,s^{-1}}$ ); in an event similar to that observed in the Bullet Cluster (Clowe et al. 2006), the dark matter halos of the galaxies pass through each other, while their dissipative baryons interact to form a new, diffuse galaxy with relatively low dark matter density (e.g., Silk 2019; Shin et al. 2020; Lee et al. 2021; Otaki & Mori 2023). However, the vigorous star formation (during which Type II SNe should dominate over Type Ia SNe) which occurs as a result of the collision to form the new galaxy should produce a relatively shallow  $[\alpha/\mathrm{Fe}]$  gradient as a function of [Fe/H] (Silk 2019), unlike the steep decline we observe for And XIX.

In the late dry-merger scenario, several mergers between small, gas-poor satellites built And XIX into an inherently diffuse galaxy (Rey et al. 2019). Since these small systems are thought to be quenched by reionization, the resulting galaxy should be very metal-poor, and—since there should be insufficient time for many Type Ia SNe to have occurred prereionization—will have a relatively shallow  $[\alpha/\text{Fe}]$  gradient as a function of [Fe/H]. This does not align with the metallicity we measure for And XIX, which is  $\sim\!2\sigma$  above the massmetallicity relation, nor the steep decline in  $[\alpha/\text{Fe}]$  we observe. Truly dry mergers also cannot easily explain the second postreionization burst of star formation in And XIX seen by C22.

In the tidal-dwarf scenario, baryonic material ejected during the interaction or merger of two massive, gas-rich galaxies becomes self-gravitating, producing a diffuse, effectively dark-matter-free galaxy (e.g., Barnes & Hernquist 1992; Duc et al. 2014; Ploeckinger et al. 2018). Since the material used to build the galaxy has already been enriched in the more massive parent system(s), a metallicity higher than that predicted by the current-day mass-metallicity relation is expected—as we observe for And XIX. However, while And XIX has a low dark matter density, its total M/L ratio is high, indicating it is still a dark-matter-dominated system (C20). This is inconsistent with the lack of dark matter associated with TDGs.

In addition, galaxies identified as TDGs in the literature are all typically young (≤4 Gyr), gas-rich, and clearly located in the tidal tails of more massive systems. While And XIX is in the vicinity of other stellar debris, as discussed in Section 5.1, there is currently no clear connection between this debris, And XIX, and M31. More critically, And XIX is both ancient (C22) and contains little to no gas (e.g., Kaisin & Karachentsev 2013), making it difficult to securely identify as a TDG. Propermotion measurements might help to establish whether And XIX was ever located near a system sufficiently massive enough to form TDGs on a timescale consistent with that of its ancient star formation history.

# 6. Summary

In this work, we present the first  $\alpha$ -abundance measurements for the diffuse M31 satellite And XIX derived from medium-resolution spectra. From data first presented in C20, we identify 86 targets which we consider to be likely And XIX members, defined here as having  $P_{\rm tot}>0.5$  and  $\Gamma/\sigma_{\Gamma}<0.2$ . We group stars with similar photometric metallities and coadd them to obtain a total of 20 independent data points. We use spectral synthesis to derive [Fe/H] and [ $\alpha$ /Fe] measurements for each coadded spectrum; these reflect the weighted average of the underlying values of the individual contributing component stars.

We find a trend of declining  $[\alpha/\text{Fe}]$  with increasing [Fe/H], as seen in other MW and M31 dSphs, indicating Type Ia SNe contribute throughout the chemical evolution of And XIX. The slope of this trend is steep  $(d[\alpha/\text{Fe}]/d[\text{Fe}/\text{H}] \sim -0.65)$ , and comparable to that in other similar-luminosity dSphs also comprised primarily of ancient stellar populations (e.g., Sex). The mean metallicity we measure for And XIX ( $[\text{Fe}/\text{H}]\sim1.5$ ) is  $\sim0.6$  dex higher than that from the existing literature, placing it  $\sim2\sigma$  above the present-day stellar mass-metallicity relation for Local Group dSphs.

Our abundance measurements do not support mergers as a formation mechanism for And XIX. Early high-speed, gas-rich mergers might explain a second burst of star formation seen in And XIX's SFH, but the resulting vigorous star formation and increased rate of Type II SNe should produce a shallow, if not flat, slope in  $[\alpha/Fe]$ –[Fe/H] space. Late dry mergers of reionization fossils are also expected to result in a relatively flat  $[\alpha/\text{Fe}]$ -[Fe/H] slope but at very low metallicity, given the lack of time for significant numbers of Type Ia SNe to occur in the component galaxies pre-reionization. The relatively high mean [Fe/H] and steep  $d[\alpha/\text{Fe}]/d[\text{Fe/H}]$  slope we measure for And XIX cannot easily be explained in these scenarios. The TDG scenario for the formation of And XIX could explain the higher than expected [Fe/H] we observe for it. However, the ancient age of And XIX and the lack of clear connection to a larger parent system make this suggestion difficult to verify.

Instead, we suggest tidal interactions as a promising avenue of formation for And XIX. We posit a scenario where And XIX was originally  ${\sim}10{\times}$  more massive than its current luminosity would suggest, allowing it to retain gas and evolve to reach a higher [Fe/H] than satellites with a similar current luminosity. Since then, it has experienced a strong tidal interaction, stripping some of its existing stellar and dark mass, explaining the low dark matter halo density observed by C20, and its diffuse structure. Either at the same time, or-more likelybeginning even earlier, And XIX's gas has also been stripped, quenching it as indicated by its SFH (C22). This relatively ancient quenching prevented the extended star formation which results in the shallow  $d[\alpha/\text{Fe}]/d[\text{Fe/H}]$  gradients usually seen in more massive systems, explaining the steep decline we observe. Proper-motion measurements that allow the orbit of And XIX to be traced are necessary to confirm the timing and intensity of any such interaction, e.g., with M31. Nevertheless, our data clearly place stronger constraints on And XIX's formation, providing new insight into this unique galaxy and those like it.

### Acknowledgments

The authors recognize and acknowledge the very significant cultural role and reverence that the summit of Maunakea has always had within the indigenous Hawaiian community. We are most fortunate to have the opportunity to conduct observations from this mountain. This research is based on observations made with the NASA/ESA Hubble Space Telescope obtained from the Space Telescope Science Institute, which is operated by the Association of Universities for Research in Astronomy, Inc., under NASA contract NAS 5-26555. These observations are associated with program ID 15302; support for this work (L.R.C and K.M.G.) was provided by NASA through grant No. HST-GO-15302. I.E. acknowledges generous support from a Carnegie–Princeton Fellowship through Princeton University.

Facilities: Keck:II(DEIMOS), Subaru(Suprime-Cam). Software: astropy (Astropy Collaboration et al. 2013, 2018, 2022), corner (Foreman-Mackey 2016), dustmaps (Green 2018), emcee (Foreman-Mackey et al. 2013), matplotlib (Hunter 2007), numpy (van der Walt et al. 2011), phew (Núñez et al. 2022), scipy (Virtanen et al. 2020).

# Appendix C19 Member Comparison

Here, we discuss differences between our And XIX sample and that of C20. There are multiple factors which contribute to the differences in membership noted in Section 2.4: (a) differing reduction methods for the data, (b) different measurement techniques used to derive the velocities and/or the EWs of the Na I lines, and (c) differing membership criteria used. We cannot disentangle the first two effects, which affect the entire underlying data set; we therefore discuss these two effects first, followed by the effect of the differing membership criteria separately.

There are no large systemic differences across the full underlying data set. Targets that are successfully reduced by both our pipeline and that of C20 have correlated LOS velocities and Na I EW measurements. We show difference histograms for the velocity and Na I EWs, scaled by the uncertainty in the differences (i.e.,  $\frac{V-V_{\rm C20}}{\sqrt{\sigma_V^2-\sigma_{V,\rm C20}^2}}$  and  $\frac{\Gamma-\Gamma_{\rm C20}}{\sqrt{\sigma_{\Gamma}^2-\sigma_{\Gamma,\rm C20}^2}}$ ) in Figure 9. Gray lines indicate the full shared sample, while solid and dashed orange lines indicate targets which we calculate as having  $P_{\rm tot}>0.5$  and  $P_{\rm tot}>0.1$  (reflecting the different  $P_{\rm tot}$  cutoffs we use compared to C20). We find that while there are certainly large tails to these distributions, particularly for likely member stars, the median differences are consistent with zero.

We now consider the effects of the different membership criteria we apply. Figure 10 presents a histogram of  $\Gamma/\sigma_{\Gamma}$  for all targets with  $P_{\text{tot}} > 0.1$  (dashed orange) and  $P_{\text{tot}} > 0.5$  (solid orange), compared to that for stars which are selected according to the membership criteria of C20 (i.e.,  $P_{\text{tot}} > 0.1$  and  $\Gamma < 2$ ) in blue. The vertical dashed black line indicates the  $\Gamma/\sigma_{\Gamma} < 0.2$ cutoff we apply to selected likely And XIX members. We find that the two membership criteria produce very similar samples, with 85% of likely members in common between the two cuts. The higher  $P_{\text{tot}}$  cutoff for our primary subsample reduces the number of likely And XIX stars by seven; as discussed in Section 2.4, we coadd these stars separately as our lowprobability subsample. All stars which have  $\Gamma < 2$  pass our  $\Gamma/\sigma_{\Gamma}$  cut, but our  $\Gamma/\sigma_{\Gamma}$  cut does result in an additional 16 stars being considered members. These stars have very low S/N, which makes any nominal measurement of their Na I absorption very uncertain. We confirm that none of these stars have visually identifiable Na I doublets.

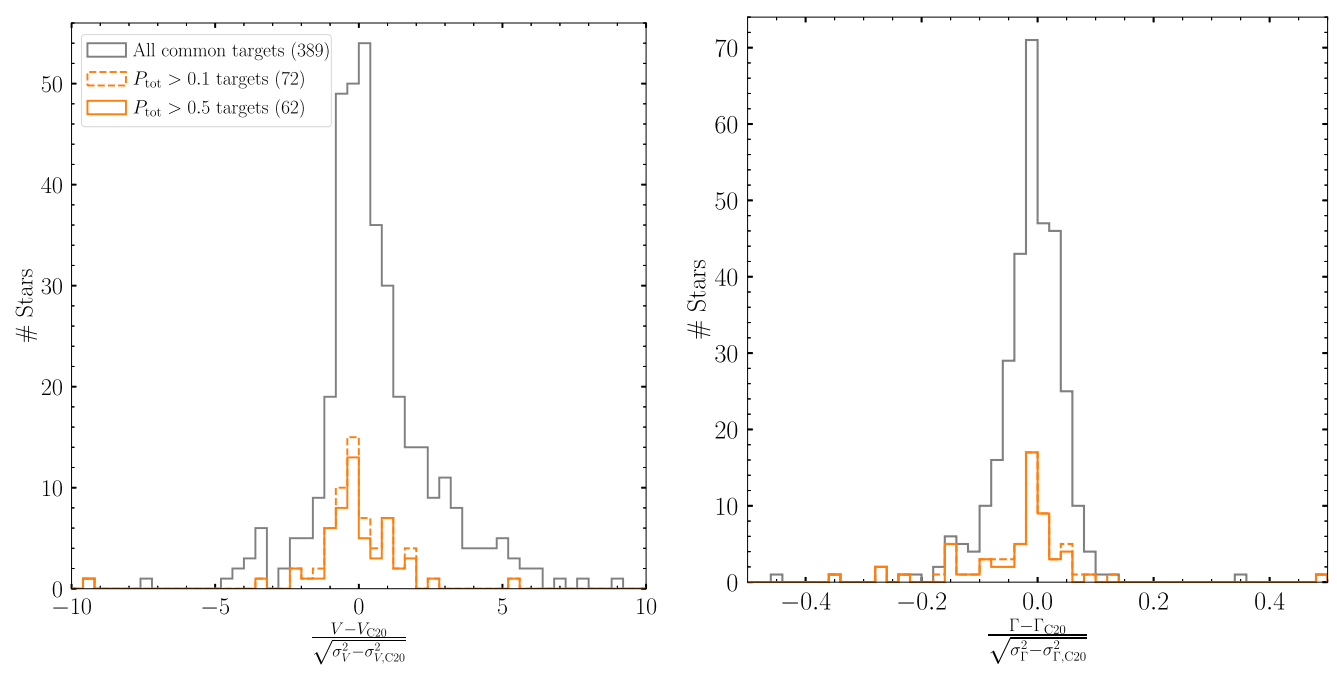
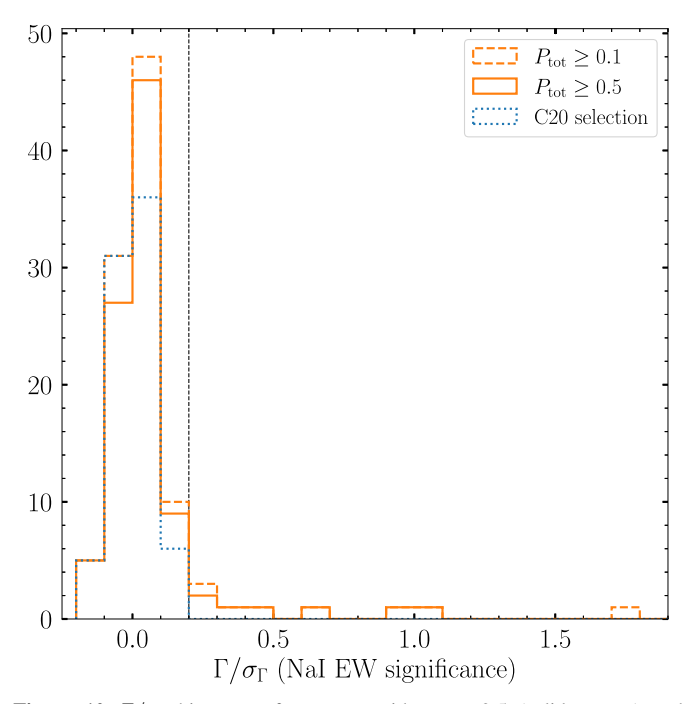


Figure 9. Normalized differences between the LOS velocity (left) and EW of the Na I doublet (Γ, right) produced from our reduction and that of C20. The gray histogram presents the differences for the entire common sample of 389 targets; the dashed orange line indicates common targets which have a  $P_{\text{tot}} > 0.1$  of being associated with And XIX (the cutoff used in C20), and the solid orange line shows common targets which have a  $P_{\text{tot}} > 0.5$  of being associated with And XIX. Stars which are likely associated with And XIX have relatively small differences in their derived velocities and Γ values derived from both reductions.



**Figure 10.**  $\Gamma/\sigma_{\Gamma}$  histogram for targets with  $P_{\rm tot}>0.5$  (solid orange) and  $P_{\rm tot}>0.1$  (dashed orange). The black dashed line indicates a  $\Gamma/\sigma_{\Gamma}$  cutoff of 0.2, which we use to select likely And XIX members. The dashed blue histogram indicates targets instead selected using the criteria described in C20, i.e.,  $P_{\rm tot}>0.1$  and  $\Gamma<2$ . All targets which pass the C20 selection also pass our  $\Gamma/\sigma_{\Gamma}$  cut.

#### **ORCID iDs**

L. R. Cullinane https://orcid.org/0000-0001-8536-0547 Karoline M. Gilbert https://orcid.org/0000-0003-0394-8377 Ivanna Escala https://orcid.org/0000-0002-9933-9551 J. Leigh Wojno https://orcid.org/0000-0002-3233-3032 Evan N. Kirby https://orcid.org/0000-0001-6196-5162 Kateryna A. Kvasova https://orcid.org/0000-0002-7438-1059

Erik Tollerud https://orcid.org/0000-0002-9599-310X Michelle L. M. Collins https://orcid.org/0000-0002-1693-3265

R. Michael Rich https://orcid.org/0000-0003-0427-8387

### References

```
Amorisco, N. C. 2019, MNRAS, 489, L22
Armandroff, T. E., & Da Costa, G. S. 1991, AJ, 101, 1329
Astropy Collaboration, Price-Whelan, A. M., Lim, P. L., et al. 2022, ApJ,
  935, 167
Astropy Collaboration, Price-Whelan, A. M., Sipőcz, B. M., et al. 2018, AJ,
Astropy Collaboration, Robitaille, T. P., Tollerud, E. J., et al. 2013, A&A,
Barnes, J. E., & Hernquist, L. 1992, Natur, 360, 715
Bennet, P., Sand, D. J., Zaritsky, D., et al. 2018, ApJL, 866, L11
Bettinelli, M., Hidalgo, S. L., Cassisi, S., Aparicio, A., & Piotto, G. 2018,
   MNRAS, 476, 71
Bressan, A., Marigo, P., Girardi, L., et al. 2012, MNRAS, 427, 127
Brown, T. M., Tumlinson, J., Geha, M., et al. 2014, ApJ, 796, 91
Carleton, T., Errani, R., Cooper, M., et al. 2019, MNRAS, 485, 382
Chan, T. K., Kereš, D., Wetzel, A., et al. 2018, MNRAS, 478, 906
Clowe, D., Bradač, M., Gonzalez, A. H., et al. 2006, ApJL, 648, L109
Collins, M. L. M., Tollerud, E. J., Rich, R. M., et al. 2020, MNRAS, 491, 3496
Collins, M. L. M., Williams, B. F., Tollerud, E. J., et al. 2022, MNRAS,
Conn, A. R., Ibata, R. A., Lewis, G. F., et al. 2012, ApJ, 758, 11
Cooper, M. C., Newman, J. A., Davis, M., Finkbeiner, D. P., & Gerke, B. F.
   2012, spec2d: DEEP2 DEIMOS Spectral Pipeline, Astrophysics Source
```

Di Cintio, A., Brook, C. B., Dutton, A. A., et al. 2017, MNRAS, 466, L1

Escala, I., Gilbert, K. M., Kirby, E. N., et al. 2020a, ApJ, 889, 177

Duc, P.-A., Paudel, S., McDermid, R. M., et al. 2014, MNRAS, 440, 1458

Code Library, ascl:1203.003 Da Costa, G. S. 2016, MNRAS, 455, 199

Dekel, A., & Silk, J. 1986, ApJ, 303, 39

```
Escala, I., Kirby, E. N., Gilbert, K. M., Cunningham, E. C., & Wojno, J. 2019,
   ApJ, 878, 42
Escala, I., Kirby, E. N., Gilbert, K. M., et al. 2020b, ApJ, 902, 51
Faber, S. M., Phillips, A. C., Kibrick, R. I., et al. 2003, Proc. SPIE, 4841, 1657
Fernandes, L., Mason, A. C., Horta, D., et al. 2023, MNRAS, 519, 3611
Font, A. S., McCarthy, I. G., Crain, R. A., et al. 2011, MNRAS, 416, 2802
Foreman-Mackey, D. 2016, JOSS, 1, 24
Foreman-Mackey, D., Hogg, D. W., Lang, D., & Goodman, J. 2013, PASP,
Gilbert, K. M., Guhathakurta, P., Kalirai, J. S., et al. 2006, ApJ, 652, 1188
Gilbert, K. M., Kirby, E. N., Escala, I., et al. 2019, ApJ, 883, 128
Gilmore, G., & Wyse, R. F. G. 1991, ApJL, 367, L55
Gómez, F. A., Besla, G., Carpintero, D. D., et al. 2015, ApJ, 802, 128
Green, G. M. 2018, JOSS, 3, 695
Hammer, F., Yang, Y. B., Wang, J. L., et al. 2018, MNRAS, 475, 2754
Hasselquist, S., Hayes, C. R., Lian, J., et al. 2021, ApJ, 923, 172
Hill, V., Skúladóttir, Á., Tolstoy, E., et al. 2019, A&A, 626, A15
Hogg, D. W., Bovy, J., & Lang, D. 2010, arXiv:1008.4686
Hunter, J. D. 2007, CSE, 9, 90
Ibata, R., Martin, N. F., Irwin, M., et al. 2007, ApJ, 671, 1591
Jackson, R. A., Kaviraj, S., Martin, G., et al. 2021, MNRAS, 502, 1785
Ji, A. P., Koposov, S. E., Li, T. S., et al. 2021, ApJ, 921, 32
Kaisin, S. S., & Karachentsev, I. D. 2013, Ap, 56, 305
Karachentsev, I. D., & Kashibadze, O. G. 2006, Ap, 49, 3
Kirby, E. N. 2011, PASP, 123, 531
Kirby, E. N., Cohen, Judith., G., Smith, G. H., et al. 2011, ApJ, 727, 79
Kirby, E. N., Cohen, J. G., Guhathakurta, P., et al. 2013, ApJ, 779, 102
Kirby, E. N., Gilbert, K. M., Escala, I., et al. 2020, AJ, 159, 46
Kirby, E. N., Guhathakurta, P., Bolte, M., Sneden, C., & Geha, M. C. 2009,
    pJ, 705, 328
Kirby, E. N., Guhathakurta, P., Simon, J. D., et al. 2010, ApJS, 191, 352
Kirby, E. N., Guhathakurta, P., & Sneden, C. 2008, ApJ, 682, 1217
Kupka, F., Piskunov, N., Ryabchikova, T. A., Stempels, H. C., &
   Weiss, W. W. 1999, A&AS, 138, 119
Kurucz, R. L. 1992, RMxAA, 23, 45
Kurucz, R. L. 1993, PhSt, T47, 110
Kvasova, K., Kirby, E. N., & Beaton, R. L. 2024, arXiv:2404.11804
Lee, J., Shin, E.-j., & Kim, J.-h. 2021, ApJL, 917, L15
Lee, M. G., Yuk, I.-S., Park, H. S., Harris, J., & Zaritsky, D. 2009, ApJ,
   703, 692
Lemasle, B., De Boer, T. J. L., Hill, V., et al. 2014, A&A, 572, A88
Macciò, A. V., Prats, D. H., Dixon, K. L., et al. 2020, MNRAS, 501, 693
```

```
Martin, N. F., Ibata, R. A., Lewis, G. F., et al. 2016, ApJ, 833, 167
McConnachie, A. W. 2012, AJ, 144, 4
McConnachie, A. W., Huxor, A., Martin, N. F., et al. 2008, ApJ, 688, 1009
McConnachie, A. W., Ibata, R., Martin, N., et al. 2018, ApJ, 868, 55
McKinnon, K. A., Cunningham, E. C., Rockosi, C. M., et al. 2023, ApJ,
Moreno, J., Danieli, S., Bullock, J. S., et al. 2022, NatAs, 6, 496
Naidu, R. P., Conroy, C., Bonaca, A., et al. 2020, ApJ, 901, 48
Newman, J. A., Cooper, M. C., Davis, M., et al. 2013, ApJS, 208, 5
Núñez, A., Douglas, S. T., Alam, M., & DeLaurentiis, S. 2022, PHEW:
  PytHon Equivalent Widths v2.0, Zenodo, doi:10.5281/zenodo.6422571
Ogiya, G., van den Bosch, F. C., & Burkert, A. 2022, MNRAS, 510, 2724
Otaki, K., & Mori, M. 2023, MNRAS, 525, 2535
Peñarrubia, J., McConnachie, A. W., & Navarro, J. F. 2008a, ApJ, 672,
Peñarrubia, J., Navarro, J. F., & McConnachie, A. W. 2008b, ApJ, 673, 226
Ploeckinger, S., Sharma, K., Schaye, J., et al. 2018, MNRAS, 474, 580
Quirk, A., Guhathakurta, P., Gilbert, K. M., et al. 2022, AJ, 163, 166
Read, J. I., Walker, M. G., & Steger, P. 2019, MNRAS, 484, 1401
Revaz, Y., Jablonka, P., Sawala, T., et al. 2009, A&A, 501, 189
Rey, M. P., Pontzen, A., Agertz, O., et al. 2019, ApJL, 886, L3
Shin, E.-j., Jung, M., Kwon, G., et al. 2020, ApJ, 899, 25
Silk, J. 2019, MNRAS, 488, L24
Simon, J. D., & Geha, M. 2007, ApJ, 670, 313
Sneden, C., Kraft, R. P., Shetrone, M. D., et al. 1997, AJ, 114, 1964
Sohn, S. T., Majewski, S. R., Muñoz, R. R., et al. 2007, ApJ, 663, 960
Starkenburg, E., Hill, V., Tolstoy, E., et al. 2010, A&A, 513, A34
Theler, R., Jablonka, P., Lucchesi, R., et al. 2020, A&A, 642, A176
Tinsley, B. M. 1979, ApJ, 229, 1046
Torrealba, G., Belokurov, V., Koposov, S. E., et al. 2019, MNRAS, 488, 2743
Van Der Marel, R. P., Besla, G., Cox, T. J., Sohn, S. T., & Anderson, J. 2012,
van der Walt, S., Colbert, S. C., & Varoquaux, G. 2011, CSE, 13, 22
Van Dokkum, P. G., Abraham, R., Merritt, A., et al. 2015, ApJ, 798, L45
Vargas, L. C., Geha, M. C., & Tollerud, E. J. 2014, ApJ, 790, 73
Virtanen, P., Gommers, R., Oliphant, T. E., et al. 2020, NatMe, 17, 261
Watkins, L. L., Evans, N. W., & van de Ven, G. 2013, MNRAS, 430, 971
Weisz, D. R., Dolphin, A. E., Skillman, E. D., et al. 2015, ApJ, 804, 136
Weisz, D. R., Martin, N. F., Dolphin, A. E., et al. 2019, ApJL, 885, L8
Wojno, J., Gilbert, K. M., Kirby, E. N., et al. 2020, ApJ, 895, 78
Wojno, J. L., Gilbert, K. M., Kirby, E. N., et al. 2023, ApJ, 951, 12
```

Woo, J., Courteau, S., & Dekel, A. 2008, MNRAS, 390, 1453